Tenth International Conference on Computational Fluid Dynamics (ICCFD10), Barcelona, Spain, July 9-13, 2018 **ICCFD10-100**

Modelling of Shock Wave–Boundary Layer Interaction Control by Wall Ventilation

O. Szulc, P. Doerffer, P. Flaszynski and T. Suresh
Corresponding author: oskar.szulc@imp.gda.pl

Institute of Fluid-Flow Machinery, Polish Academy of Sciences.

Abstract: The normal shock wave–boundary layer interaction (SBLI) phenomenon is known to constitute a main factor limiting the aerodynamic performance in many aeronautical applications (transonic wings, helicopter rotor blades, compressor and turbine cascades). The interaction process highly disturbs the boundary layer, often causing flow separation and onset of large scale unsteadiness (e.g. airfoil buffet or supersonic inlet buzz). In certain conditions it may also initiate a dramatic increase of acoustic emission levels (e.g. high-speed impulsive noise). To limit the negative impact of the phenomenon various flow control strategies (SBLIC) are often implemented, here in form of a passive control system realised by placing a shallow cavity covered by a perforated plate just beneath the shock. Details of the flow structure obtained by this method are studied numerically. Three distinctive experimental set-ups are considered with the interaction taking place: on a flat wall (transonic nozzle, ONERA), on a convex wall (curved duct, University of Karlsruhe), and on an airfoil (NACA 0012, NASA Langley). Depending on the relative cavity length the ventilation process leads to a transformation of the normal shock topology into: a large λ-foot structure (classical, short), a system of oblique waves (extended), or a gradual compression (full-chord). The reference and flow control cases are simulated with the SPARC code (RANS) with Spalart–Allmaras (SA) turbulence and Bohning–Doerffer (BD) transpiration models. The results are compared with the measurements, emphasizing the streamwise evolution of the boundary layer profiles and integral parameters during the interaction. Such comparisons are rarely presented even for the reference cases (SBLI), not mentioning the passive control arrangements (SBLIC).

Keywords: CFD, Transonic Flows, SBLI, SBLIC, Transpiration Modelling, Perforated Walls.

1 Introduction

Recently, a significant research effort is directed towards the flow control aiming at performance gains or noise reduction. In transonic and supersonic regimes the most significant factor is a generation of a normal shock wave. The compression not only introduces a wave drag component, but also considerably disturbs the incoming turbulent boundary layer, frequently causing separation and onset of global unsteadiness (e.g. supersonic air-intake buzz or wing buffet). The classical method of passive control of shock wave–boundary layer interaction, investigated in the Euroshock [1] and Euroshock II [2] European projects, is based on an application of a shallow cavity covered by a perforated plate locally just beneath the interaction region. Combined upstream blowing and downstream suction transform the normal shock into a large λ-foot structure. Such a process reduces the wave component of drag, and stabilizes the position of the shock. Unfortunately, due to the upstream blowing from the cavity into the main stream the boundary layer is often subjected to a forced separation. As a result a slight increase of total drag is observed for most configurations.

A physical modelling of the transpiration flow through the perforation holes proves to be a difficult task. Extensive and time-consuming efforts, undertaken by the Euroshock and Euroshock II projects consortia, led to a formulation and validation of the empirical BD transpiration law [3]. In principle, it should be possible to resolve the flow in discrete perforation holes without any need for the ventilation modelling. It turns out that having thousands of such holes it is not feasible to resolve the requested flow details with current CFD techniques and available computer resources. It is necessary to rely on a transpiration model, usually implemented in the solver as a perforated wall boundary condition or a source/sink term. Despite the definite success of the BD law (and its general worldwide use) the published thus far results of the numerical simulations involving the shock wave–boundary layer interaction control (SBLIC) by passive wall ventilation are still not satisfactory, and reveal many discrepancies in comparison with the available experimental data.

This article covers the details of a revised validation of the numerical implementation of the BD transpiration model in the academic, RANS flow solver SPARC. The process is based on a solution of the SBLIC phenomenon for three distinctive flow configurations, involving the classical, extended, and global passive control device arrangements. The conventional (classical) interaction control is studied in the transonic nozzle with a flat wall equipped with a relatively short cavity (ONERA) [4]. It is designed to locally transform a normal shock wave into a large λ-foot topology with an aim of wing drag reduction. In contrast, the extended version of the device is based on a prolongation of the cavity length. The normal shock is substituted with a system of much weaker oblique waves reflecting between the surface and the edge of the supersonic region. This set-up is investigated in the curved duct of the University of Karlsruhe [5]. The extreme shock structure alteration may be used for the high-speed impulsive noise reduction of helicopter rotors, but not without its performance penalties [6]. Finally, when the cavity covers the entire suction side of the airfoil (global), the resulting ventilation constitutes a suitable technique of adaptation of the effective surface shape to flow conditions. This method is tested on the NACA 0012 airfoil equipped with a full-chord perforation (NASA Langley) [7]. It is evident that even the reference configurations under low to moderate Mach numbers (without noticeable flow separation) pose a significant challenge to numerical methods and turbulence modelling, often leading to poor correlations or wrong solutions (e. g. known issue of nonphysical, asymmetric eruption of corner separation). Under transpiration flow conditions the problem is even more severe. Still, the presented RANS (SA) solutions agree relatively well with the available experimental data.

2 Passive Control of Shock Wave by Wall Ventilation

A shallow cavity covered by a perforated surface, located just beneath the shock wave–boundary layer interaction region, significantly alters the flow topology due to the occurrence of a transpiration through the plate (Figure 1). The depicted transformation of the shock system on the NACA 0012 profile was obtained at exemplary inflow conditions: Mach number $Ma_\infty = 0.8$, Reynolds number $Re_\infty = 9 \cdot 10^6$, and incidence $\alpha = 1°$. The method of control is passive in nature, and does not require any external supply of energy. The cavity connects zones of low and high pressure, located upstream and downstream of the shock wave. Upstream of the shock wave pressure in the cavity is higher than in the flow-field, leading to a blowing into the main stream. An opposite situation arises downstream of the shock wave where lower pressure in the cavity induces a suction. The blowing is perceived by the main, supersonic stream as a ramp (or a bump) resulting in a generation of a front, oblique compression which, in case of the "classical" passive control, intersects the normal shock wave, creating a large λ-foot structure (blue colour in Figure 1). The suction of the boundary layer downstream of the interaction is not sufficient to counteract the negative influence of blowing. Therefore, the final effect is a balance between two opposing trends: the growth of viscous losses (on account of boundary layer disturbance) and the reduction of wave losses (through a replacement of a normal shock by a λ-foot). It was proven during the Euroshock project that for specific configurations the "classical" passive control is capable of marginally improving the aerodynamic performance of an airfoil in transonic conditions.

An another attitude (undertaken in our research group) towards the airfoil performance has to be considered in respect to the rotor blade of a helicopter. In a high-speed forward flight the most negative effect is a generation of the shock wave which is responsible for the high-speed impulsive (HSI) noise emission. In contrast to the "classical" passive control it is proposed to limit the shock intensity by a prolonged cavity covered by a perforated plate (i.e. "extended" passive control marked in red colour in Figure 1). The induced flow recirculation through the cavity leads to a substitution of the strong, normal compression by a system of weaker, oblique waves reflecting between the surface and the edge of the supersonic region. As a result the static pressure variation in the volume above the suction side of the profile is reduced – counteracting the main source of the HSI noise. Without any modification to the outer blade tip shape nor section the extent of the supersonic area is significantly restricted, together with the maximum Mach number in the flow-field.

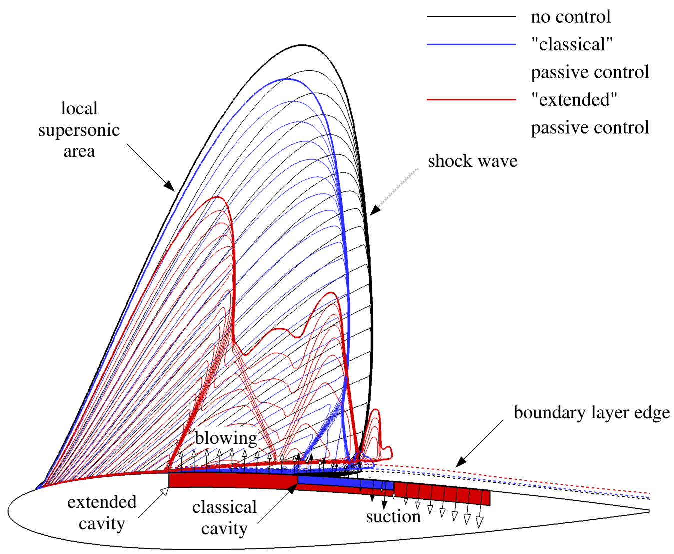

Figure 1: “Classical” and “extended” variants of passive control of shock wave by wall ventilation

3 Physical and Numerical Modelling

One of the main achievements of the Euroshock project is a development of the BD transpiration law [3]. This empirical model describes a relation between the pressure difference over the perforated plate and the induced mass flow rate. The experiments proved that the pressure in the cavity p_{c} may be considered as constant. The determination of the pressure difference $\Delta p = p\left(x\right) - p_{\mathrm{c}}$ requires the wall pressure distribution in the main stream $p\left(x\right)$. According to the BD formulation designed for passive control of the shock wave the effective Mach number in a single perforation hole Ma_{h} is calculated locally based on the expression: $Ma_{\mathrm{h}} = \left(\left|\Delta p\right| / p_0\right)^{0.55}$ where p_0 denotes the stagnation pressure value at the inlet side of the orifice, different for blowing ($\Delta p < 0$) and suction ($\Delta p > 0$). Knowing the aerodynamic (effective) porosity of the perforated plate p_{aero} (depending on the flow direction due to a low manufacturing quality of the holes) the corresponding mass flow rate of air is estimated. A passive character of the interaction is reflected in an instantaneous zero net mass-flux through the ventilated surface area. As a result an effective transpiration velocity U_{t} (normal to the wall) distribution is determined, and applied in the numerical simulation as a boundary condition.

The present investigation has been carried out with a cell-centred, block-structured code SPARC [8]. It solves numerically the compressible, Favre-averaged Navier–Stokes equations with several 0-, 1-, and 2-equation turbulence models. The shock wave–boundary layer interaction phenomenon under the influence of the transpiration is fairly predicted by a low-Reynolds closure of SA. The numerical algorithm is based on a semi-discrete scheme, utilizing the finite-volume formulation for the spatial discretization (central, 2$^{\mathrm{nd}}$ order) and the multistage, explicit Runge-Kutta approach for the integration in time (to a steady state). To damp numerical oscillations and to assure a high resolution of discontinuities (such as shock waves) the artificial dissipation model SLIP is implemented. In order to increase the convergence rate the local time-stepping, implicit residual averaging, and full-multigrid techniques are incorporated in the solver.

A perforated wall boundary condition, designed towards the modelling of passive control of the shock wave–turbulent boundary layer interaction, has been implemented in the SPARC code. In case of the classical impermeable (no-slip) wall boundary condition the tangential and normal velocity components (mean and fluctuating), as well as the eddy viscosity, are set to zero at the surface as a consequence of the adhesion of fluid. In an adiabatic flow (no wall heat-flux) pressure and density are extrapolated from the interior of the computational domain. A construction of the ventilated wall boundary condition is analogous, taking into account a non-zero normal (transpiration) velocity U_{t}, estimated from the BD law in accordance with the local properties of the main stream, i.e. pressure $p\left(x\right)$ and temperature $T\left(x\right)$. The pressure in the cavity p_{c} is assumed uniform, adapting itself naturally to ensure vanishing of the total mass flow rate through the perforated plate (passive environment). The temperature in the control system T_{c} is fixed to the stagnation value of the free-stream. If $U_\mathrm{t} = 0$, then the standard no-slip wall boundary condition is restored, allowing for modelling of the perforated and solid surfaces in a common framework. In case of the relative reference frame (helicopter rotor) an extension of this approach is required. For each section of the blade the stagnation pressure p_0 and temperature T_0 of the incoming air depend on the radial location. In such conditions the application of passive control would induce an undesirable spanwise flow inside the cavity towards the tip. To counteract this effect it was proposed to divide the cavity volume into smaller, independent and sealed sub-domains, each experiencing a quasi-2d, chordwise recirculation (more details in [6]).

When the BD model is applied for an estimation of the transpiration intensity U_t, an accurate prediction of the shock wave location and wall pressure distribution in the interaction region is required. As a consequence, a suitable correlation of the numerical results with the measurements for the reference cases (no control) is of an utmost importance. It is not an issue for internal flows (in transonic nozzles or ducts) where the shock position might be adapted by a proper choice of the value of the outlet static pressure. On the contrary, the chordwise shock location on an airfoil (or a rotor blade) is fixed for given flight conditions, leaving almost no room for any adaptation. It was found that the application of whichever of more advanced 2-equation K-τ turbulence models implemented in SPARC (e.g. Speziale–Abid–Anderson) resulted in a shock wave position significantly shifted downstream compared to the measurements of the reference NACA 0012 airfoil. Additionally, the interaction of the transpiration flow with the main stream was too intensive (e.g. nozzle with a flat wall), creating a nonphysical compression followed by an expansion at the leading edge of the perforated plate, not observed during the wind tunnel campaign. For these two reasons the calculations using 2-equation K-τ closures were abandoned in favour of a less complex 1-equation SA turbulence model. Even for SA the application of blending (buffer) zones at the upstream and downstream edges of the perforated plate was necessary to capture correctly the front, oblique shock location and wall pressure distribution, improving the coincidence of the CFD and experimental results.

4 Transonic Nozzle with Flat Wall

The first studied test case is a quasi-two-dimensional flow in the transonic nozzle (investigated experimentally during the Euroshock project by ONERA in Meudon S8 wind tunnel in France [4]) with the interaction process taking place on the flat, lower wall (Figure 2). It was equipped with a 70 mm cavity covered by a 1 mm thick perforated plate (marked as number 2) of nominal porosity $p_\mathrm{nom} = 5.7\%$ (6700 normal holes of a diameter of 0.3 mm). The test section width (distance between the side walls) was 120 mm. The LDV (Laser Doppler Velocimetry) method was applied for the investigation of the instantaneous velocity vector components U_x and U_y. Schlieren photographs delivered the visualizations of the shock wave topology. Pressure was measured at the lower wall (p), in the symmetry plane of the nozzle, and at the bottom of the cav-

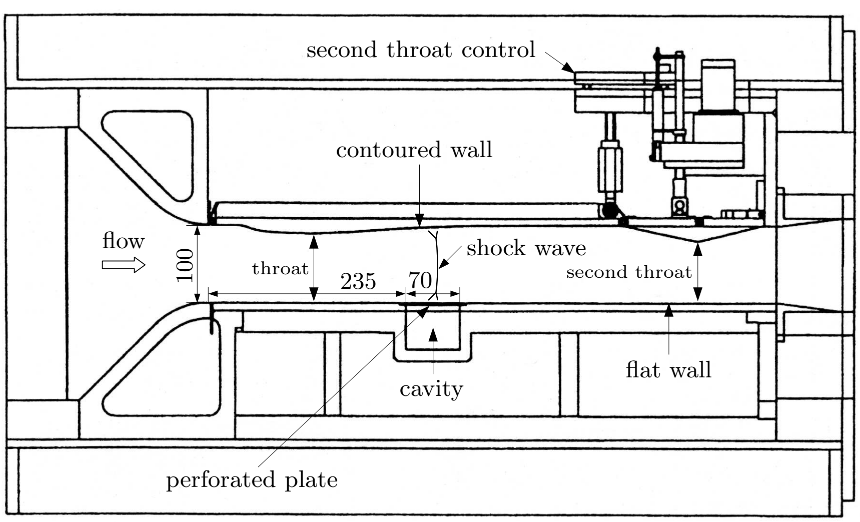

Figure 2: Transonic nozzle with flat wall (ONERA Meudon)

ity (p_c). In effect, the mean and fluctuating velocity components and turbulent shear stress R_{xy}^{turb}, as well as the streamwise development of the boundary layer integral parameters: δ^*, θ, and H were calculated. The measured velocity at the distance of 0.3 mm from the perforated plate was assumed to be the transpiration velocity U_t. The stagnation values of pressure p_0 and temperature T_0 of air entering the test section were equal to 95 000 Pa and 300 K. The turbulence level at the inlet was unknown. A normal shock wave (with the shock upstream isentropic Mach number of $Ma_{\text{is}} = 1.33$) was positioned above the cavity centre. The incoming turbulent boundary layer thickness δ upstream of the interaction zone was approx. 4 mm.

The computational domain consisted of the central part of the test section alone, modelling of the inlet and second throat was not necessary (Figure 3). Only half of the nozzle was modelled in 3d utilizing the symmetry boundary condition, therefore the distance between the side wall and the symmetry plane was 60 mm, equal to 50% of the channel width 120 mm. The shock upstream isentropic Mach number $Ma_{\text{is}} = 1.33$ did not lead to a development of a significant flow separation zone. The origin of the coordinate system was positioned in the throat ($x = 0$ mm), while the cavity covered by a perforated plate was located between $x = 130$ mm and $x = 200$ mm. It was found that the generation of a computational grid of very high spatial resolution led to the appearance of a nonphysical secondary flows intensification and eruption of corner separation. In such conditions the interaction of the shock wave with the disturbed boundary layer prevented any reasonable solutions. This issue does not occur neither in 2d (no 3d structures present) nor in 3d when the computational mesh is of low to medium density. The obtained topology, often excessively asymmetric, is not confirmed experimentally. The main reason of such behaviour was identified to be the linear eddy viscosity (Boussinesq) concept which constitutes a basis for all turbulence models available in SPARC. Application of a more advanced EARSM (Explicit Algebraic Reynolds Stress Model) or full RSM (Reynolds Stress Model) closure proved to resolve the aforementioned issue (FLOWer code from DLR in Germany). Turbulence models of a similar level of complexity are not yet available in SPARC. Instead, an another, engineering approach was undertaken, that is to locally chamfer all streamwise corners of the three-dimensional transonic nozzle geometry. It assured a proper flow behaviour in the critical regions upstream and above the passive control system, limiting the secondary flows and corner separation growth to an acceptable level.

A base 3d mesh with standard resolution of $153 \times 129 \times 65$ ($1.2 \cdot 10^6$ volumes) was modified by a local grid refinement (8 times) of block 2, containing the shock wave–boundary layer interaction and wall ventilation regions (highlighted in red colour in Figure 3), and designated $153 \times 129 \times 65+$ ($4.9 \cdot 10^6$ volumes). For comparison purposes a globally refined (8 times) mesh $307 \times 257 \times 129$ ($10.0 \cdot 10^6$ volumes)

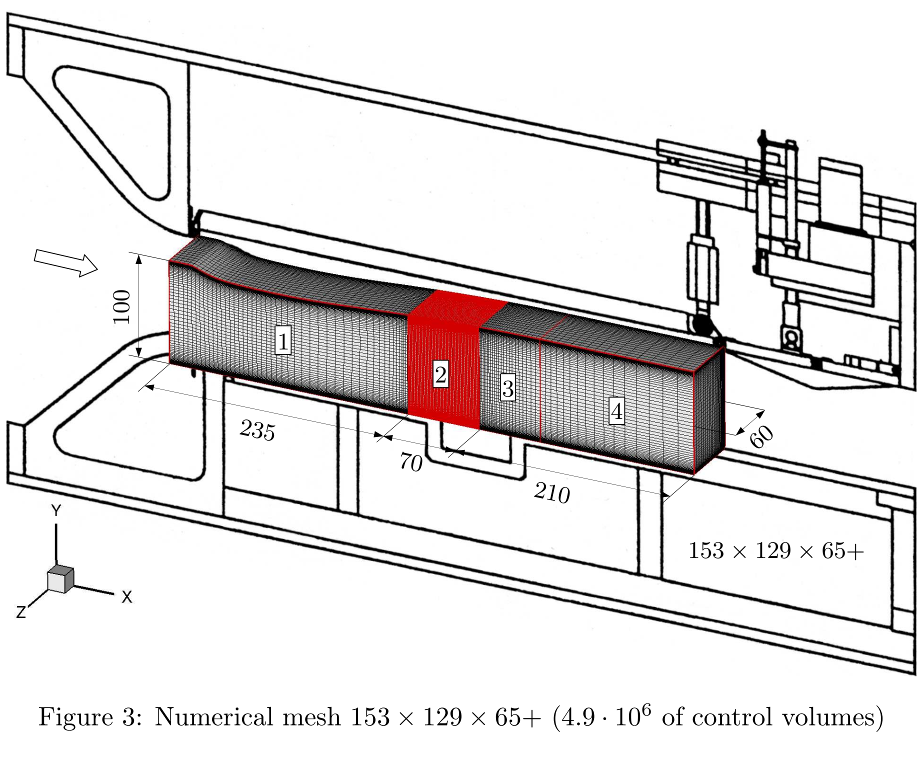

Figure 3: Numerical mesh $153 \times 129 \times 65+$ ($4.9 \cdot 10^6$ of control volumes)

was generated. A 2d grid $153 \times 129+$ was created through an extraction of the symmetry plane from the 3d model $153 \times 129 \times 65+$. The vertical size of the first layer of cells in the near-wall region was set to $\Delta y \leq 2 \cdot 10^{-6}\,\mathrm{m}$ ($y^+ \ll 1$). At the nozzle inlet the stagnation parameters boundary condition was applied with total pressure $p_0 = 95\,000\,\mathrm{Pa}$ and total temperature $T_0 = 300\,\mathrm{K}$, together with two flow angles $\alpha = \beta = 0°$, and the eddy viscosity ratio $\mu_{\mathrm{turb}}/\mu_{\mathrm{lam}} = 1$. Due to an absence of the second throat the position of shock was determined by the static pressure p value at the outlet ($61\,400\,\mathrm{Pa}$ in 2d and $58\,120\,\mathrm{Pa}$ in 3d). For three external solid walls (no-slip) the impermeable and adiabatic surface boundary condition was applied, interchanged with the perforated (permeable) wall boundary condition (nominal porosity of $p_{\mathrm{nom}} = 5.7\%$) in the passive control region. The temperature in the cavity T_{c} was kept constant at $300\,\mathrm{K}$. The convergence criteria was based on a 5 orders of magnitude reduction of the density residual, accompanied by a stabilisation of the aerodynamic forces acting on the walls and, in case of the passive control, of the cavity pressure p_{c}. The grid dependency study (adopting a solution of the reference flow), based on the comparison of wall pressure and friction coefficient distributions, proved that the locally refined grid $153 \times 129 \times 65+$ delivered accuracy of the globally refined mesh $307 \times 257 \times 129$ with half the number of cells.

Experimental schlieren photographs (depicted in Figure 4) present the effect of the "classical" passive control on the flow structure. The reference case corresponds to a normal shock wave–turbulent boundary layer interaction phenomenon at a moderate isentropic Mach number $Ma_{\mathrm{is}} = 1.33$ that is directly calculated based on the values of the minimum of wall pressure distribution p and the stagnation pressure p_0 at the inlet face of the nozzle (Figure 4a). The compression is normal almost in the entire cross-section of the tunnel. The beginning of the formation of a small λ-foot is noticeable near the lower and upper walls. Blowing from the upstream half of the cavity into the main stream highly disturbs the incoming boundary layer

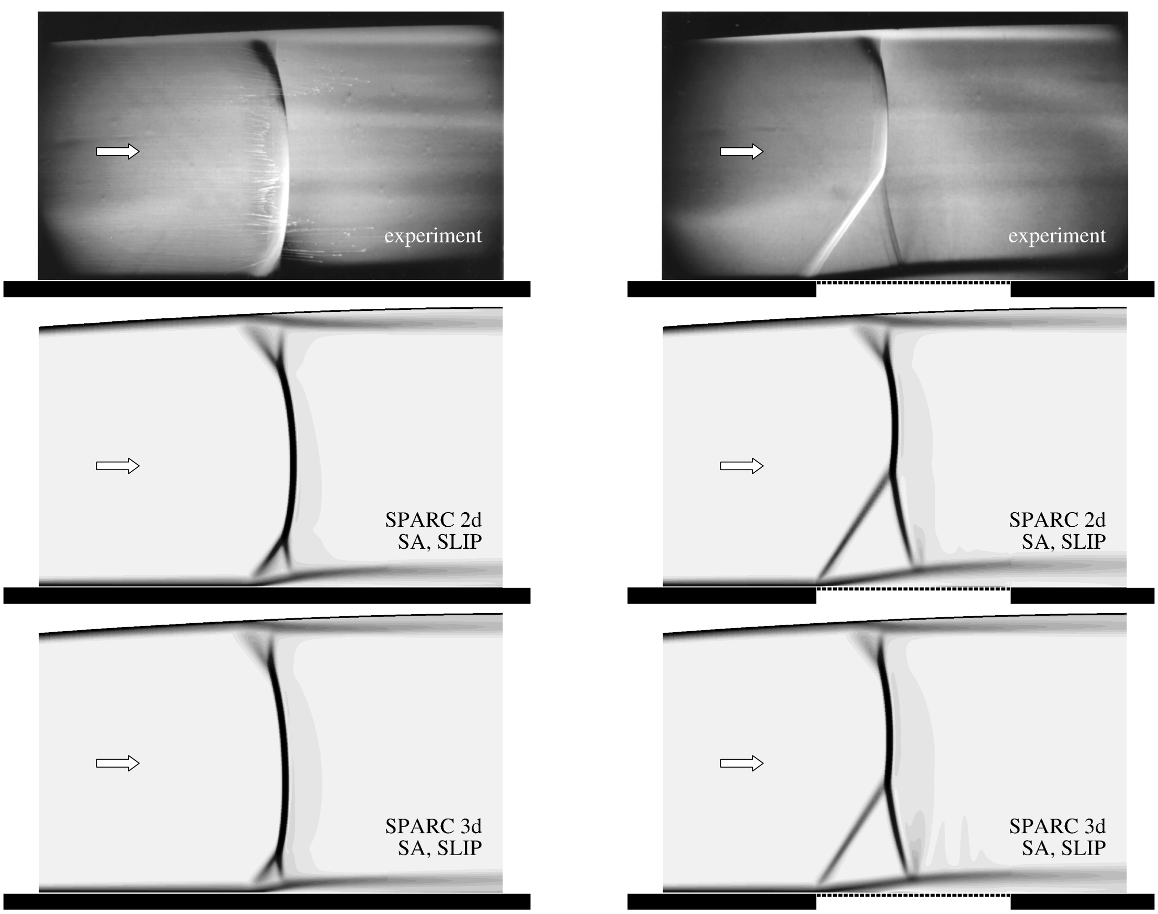

(a) reference

(b) passive control

Figure 4: Experimental schlieren photographs and 2d/3d CFD solutions ($Ma_{\mathrm{is}} = 1.33$)

(Figure 4b). The supersonic ramp effect is responsible for a generation of the front, oblique compression at the junction of the solid and perforated walls which intersects the main, normal shock creating a large λ-foot structure. At the same time the isentropic Mach number drops to $Ma_{\mathrm{is}} = 1.28$, which is a consequence of the upstream shift of the initial compression. The suction present in the downstream half of the perforated plate is not strong enough to counteract the negative disturbance introduced by the upstream blowing. The splitting of the strong, normal shock into two weaker compressions ensures a reduction of the wave losses. Unfortunately, it is accompanied by a thickening of the boundary layer and increased viscous losses.

Figure 4 contains numerical counterparts of the discussed schlieren photographs in a form of modulus of the gradient of density ρ vector in the symmetry plane of the nozzle, based on the 2d and 3d results. The visualisations faithfully replicate the experimental topology transformation. Lack of side walls in the 2d model results in a slightly higher expansion of the reference flow ($Ma_{\mathrm{is}} = 1.34$), which is the main reason of a larger λ-foot size and higher destabilization of the boundary layer downstream of the interaction compared to the 3d solution ($Ma_{\mathrm{is}} = 1.32$). Due to the appearance of the transpiration the normal shock wave is interchanged with a system of front, oblique and rear, normal compressions, which reduces losses related to a sudden drop of velocity from supersonic to subsonic value. In parallel, the shock upstream Mach number is limited to $Ma_{\mathrm{is}} = 1.29$ in 2d and $Ma_{\mathrm{is}} = 1.28$ in 3d. The disturbing action of the bleeding weakens the shear stress at the wall, reducing the tangential component of the aerodynamic force due to viscosity.

The flow recirculation through the cavity, in the opposite direction to the main flow, forces an equalization of the bottom wall pressure p/p_0 distribution between regions situated just upstream and downstream of the shock wave (Figure 5). The presented solutions are obtained with the help of special blending (buffer) zones of 5 mm length placed at the front and rear extremities of the perforated plate. Such modification of the transpiration velocity ensures a smoother transition of the flow parameters along both junctions of the permeable and impermeable surfaces. The pressure in the cavity p_{c} is stabilising naturally, ensuring a zero net mass-flux (i.e. blowing plus suction) through the ventilated surface at any given time. It is assumed that the unknown temperature in the cavity T_{c} is constant and equal to the stagnation temperature at the inlet $T_0 = 300\,\mathrm{K}$. The results of the numerical simulations agree well with the measurements (particularly in 3d) in the supersonic part of the nozzle ($0\,\mathrm{mm} < x < 130\,\mathrm{mm}$) and in the interaction domain, just above the surface of the perforated wall ($130\,\mathrm{mm} < x < 200\,\mathrm{mm}$). Downstream of the passive control system ($x > 200\,\mathrm{mm}$) a slight discrepancy is still noticeable that is a residue of the initial secondary flows intensification and eruption of corner separation issue, solved by a modification of the original duct geometry (corners

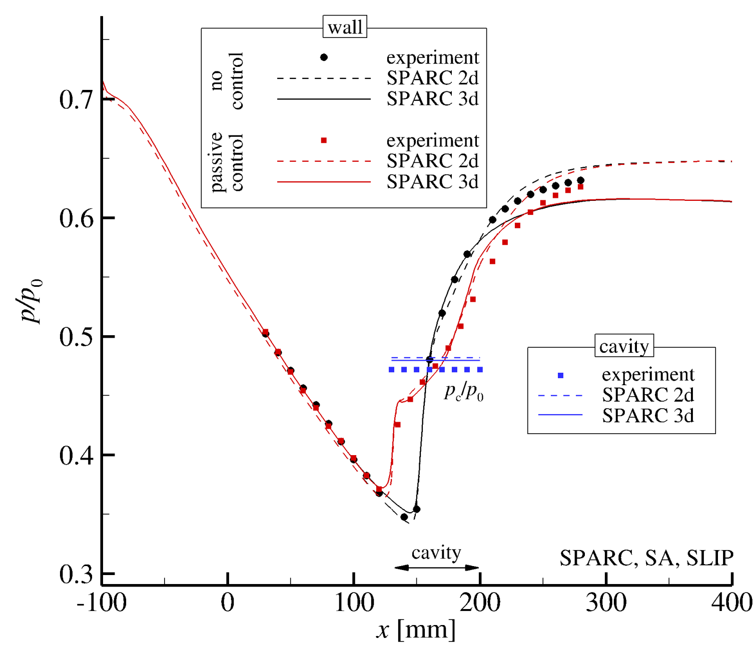

Figure 5: Bottom wall pressure p/p_0 distribution

chamfering). That is also an additional reason why the 2d and 3d solutions significantly differ in this area, apart from the apparent lack of side wall boundary layers in the 2d model. The measured value of pressure in the cavity system $p_c/p_0 = 0.472$ is captured by the 2d ($p_c/p_0 = 0.482$) and 3d numerics ($p_c/p_0 = 0.480$), with a deviation reaching approx. 2%. In case of the controlled flow modelled in the full, three-dimensional geometry of the nozzle a lack of buffer zones shifts the location of the initial oblique compression by 5 mm upstream which seems now to start too early regarding the recorded wall pressure p/p_0 distribution.

It was evident that the application of any more complex 2-equation K-τ turbulence model implemented in SPARC (e.g. Speziale–Abid–Anderson) results in a much larger deviation compared with the experimental points (not shown here). A too strong interaction of the incoming supersonic stream with the blowing out from the cavity at the leading edge of the perforated plate caused a too intensive compression, followed by a deep plateau – a flow pattern that is not confirmed by the wind tunnel tests in which the deceleration was more gradual. As an additional verification of the impact of 3d structures on the transpiration the cavity volume was divided into a few streamwise sections (the approach designed for a helicopter rotor blade). The resultant flow parameters extracted from the symmetry plane of a nominally 2d nozzle were identical as in case of a single cavity volume. This acknowledged a negligible level of the cross-wise recirculation in the cavity, meaning no transpiration velocity variation across the channel width. Additionally, taking into account the stabilisation process of the temperature in the cavity T_c resulted in a value that is only 3 K lower than the stagnation temperature at the inlet $T_0 = 300$ K, which sanctions the initial assumption.

Figure 6 presents contour maps of Mach number Ma in the symmetry plane of the nozzle, in a rectangular zone that is stretching from 15 mm upstream to 60 mm downstream of the passive control system, and up to a distance of 21 mm from the wall (LDV window). The non-dimensional parameter Ma is calcu-

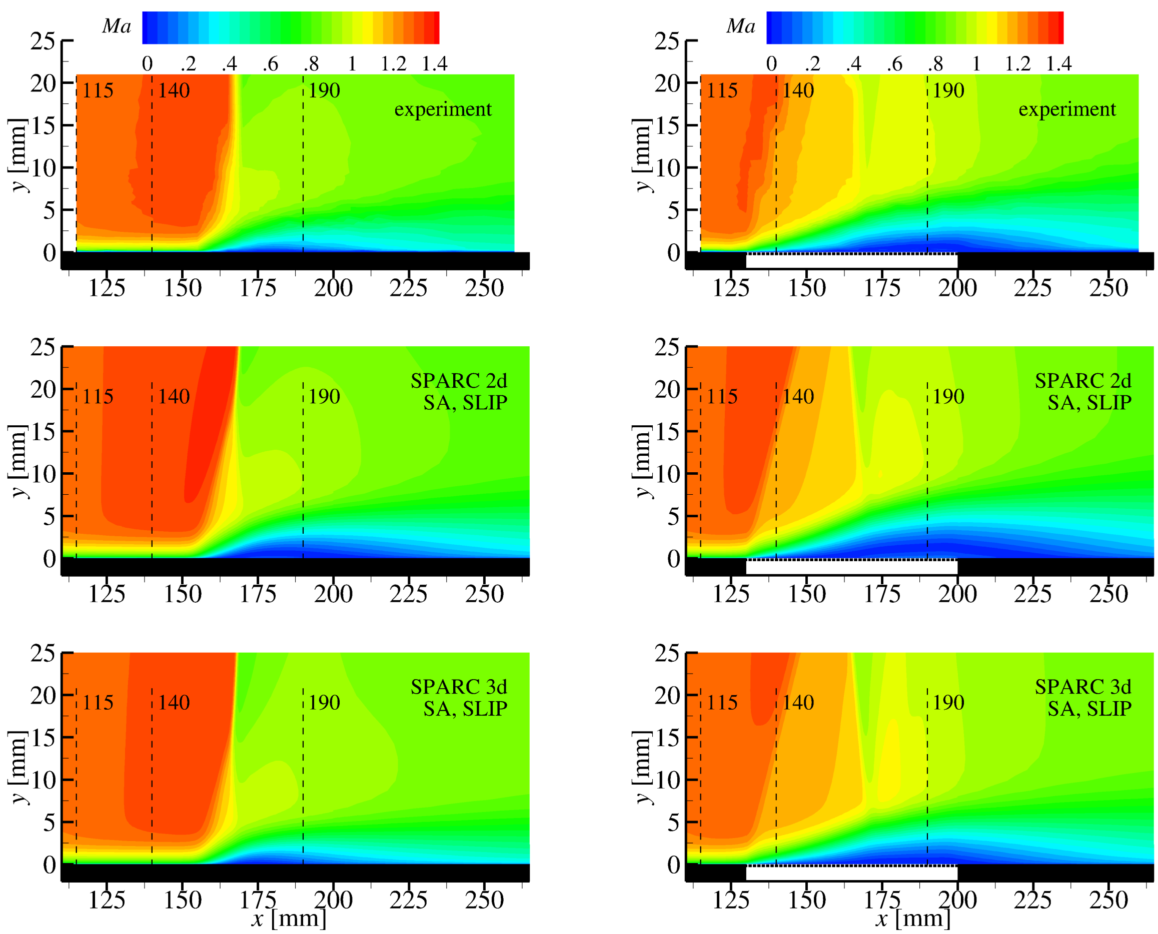

(a) reference

(b) passive control

Figure 6: Experimental (LDV) and numerical (2d/3d CFD) contour maps of Mach number Ma

lated based on the modulus of a two-dimensional velocity vector U (isentropic relations) with an assumption of a constant stagnation temperature in the whole flow-field (equal to the inlet value, i.e. $T_0 = 300\,\mathrm{K}$):

$$Ma = \frac{U}{\sqrt{\gamma R T}} \quad , \qquad T = T_0 - \frac{\gamma - 1}{\gamma R}\,\frac{U^2}{2} \tag{1}$$

where γ and R symbolize the specific heat ratio and the gas constant of air respectively. For the reference case (Figure 6a) the displayed maximum Mach number reaches: 1.34 (LDV measurement), 1.36 (2d), and 1.33 (3d). A visualisation of the experimental velocity field indicates no boundary layer separation (within a low near-wall accuracy of the LDV method). Numerical results reveal that a very oblate reversed flow region is positioned between $x = 161\,\mathrm{mm}$ and $x = 215\,\mathrm{mm}$ (height of 0.6 mm) in 2d and between $x = 163\,\mathrm{mm}$ and $x = 186\,\mathrm{mm}$ (height of 0.1 mm) in 3d. When passive control is activated (Figure 6b) the maximum Mach number drops to: 1.32 (LDV), 1.32 (2d), and 1.30 (3d). This time even the test data point out the appearance of a separation area located between $x = 169\,\mathrm{mm}$ and $x = 205\,\mathrm{mm}$ (height of 0.6 mm). The numerical simulations confirm the existence of the reversed flow region situated between $x = 140\,\mathrm{mm}$ and $x = 236\,\mathrm{mm}$ (height of 1.3 mm) in 2d and between $x = 145\,\mathrm{mm}$ and $x = 213\,\mathrm{mm}$ (height of 0.4 mm) in 3d. A larger size of the predicted separation bubble is a consequence of an insufficient resolution of the LDV method.

Figure 7 presents contour maps of turbulent (Reynolds) shear stress $R^{\mathrm{turb}}_{xy}/\rho\, U^2_{\mathrm{ref}}$ in the symmetry plane of the nozzle, in the above defined LDV window. The normal components of the turbulent stress tensor (available in 2d from the experiment) are not analysed here since the SA model does not include the turbulent kinetic energy term in the Boussinesq approximation, therefore it cannot model its impact on the solution.

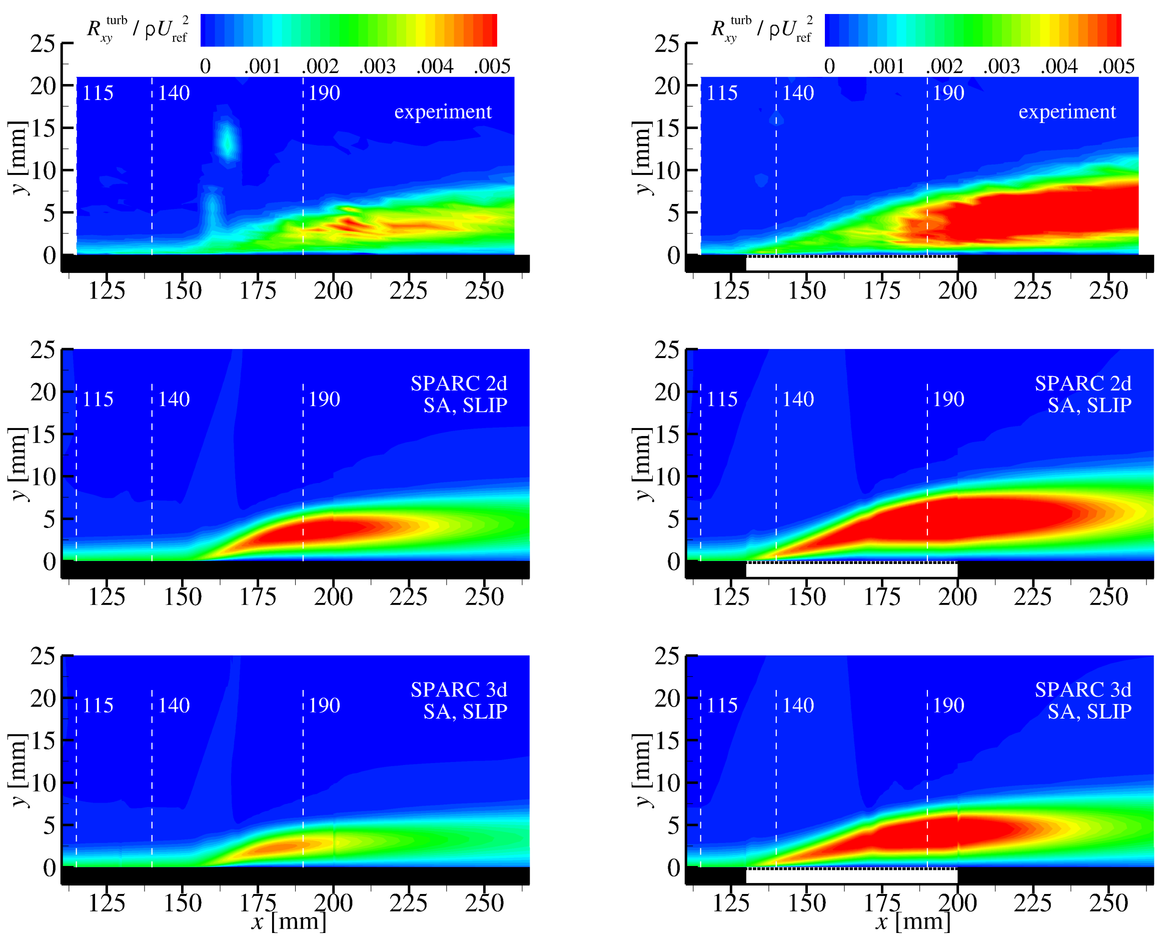

(a) reference

(b) passive control

Figure 7: Experimental (LDV) and numerical (2d/3d CFD) contour maps of turbulent stress $R^{\mathrm{turb}}_{xy}/\rho\, U^2_{\mathrm{ref}}$

The given values of R_{xy}^{turb} are referenced to the air density $\rho_{\mathrm{ref}} = 0.563\,\mathrm{kg\,m^{-3}}$ and velocity $U_{\mathrm{ref}} = 377\,\mathrm{m\,s^{-1}}$ squared at a point located 15 mm upstream of the cavity, at the boundary layer edge. For an adiabatic flat plate flow with $Ma < 5$ a difference between compressible (mass-weighted Favre averaging used in SPARC) and incompressible (Reynolds averaging used in the LDV data post-processing) correlations is small, and may be neglected. For the reference case (Figure 7a) the shock wave–boundary layer interaction process leads to an enhanced turbulence intensity that not only increases the mixing area considerably, but also amplifies (approx. 2 times) the maximum values of R_{xy}^{turb}. The effect of passive control is felt mainly because of the existence of blowing from the cavity that destabilises the boundary layer, rising the turbulent fluctuations even further (Figure 7b). The maximum value of $R_{xy}^{\mathrm{turb}}/\rho\, U_{\mathrm{ref}}^2 = 0.0052$ (registered in the LDV zone) increases up to 0.0072 (by 37%), shifting its position downstream by 25 mm (from $x = 205\,\mathrm{mm}$ to $x = 230\,\mathrm{mm}$) and off the wall by 2.6 mm (from $y = 3.9\,\mathrm{mm}$ to $y = 6.5\,\mathrm{mm}$). Computational model predicts the location of these extrema in the region located near the trailing edge of the perforated plate (between $x = 180\,\mathrm{mm}$ and $x = 200\,\mathrm{mm}$). This behaviour may be explained by a rapid coarsening of the numerical grid just downstream of the very refined interaction area ($x > 200\,\mathrm{mm}$) which determines the precision of calculation of the velocity gradient, and hence of the Reynolds shear stress. The simulations suggest a similar increase of the maximum of $R_{xy}^{\mathrm{turb}}/\rho\, U_{\mathrm{ref}}^2$ by 35% in 2d and by 47% in 3d, with a shift from the surface equal to 1.7 mm and 2.1 mm respectively. It is worth to mention that a relatively high measurement uncertainty of the LDV method (of the order of 10% of U_{ref}) may have a substantial impact on the presented comparisons.

The measured and calculated transpiration velocity U_{t} distributions over the perforated plate length L are depicted in Figure 8. There is a remarkable agreement of the 3d solution with the experimental points in the downstream part of the passive control system ($x/L > 0.6$) where suction ($U_{\mathrm{t}} < 7.5\,\mathrm{m\,s^{-1}}$) is present. The 2d model is only slightly less accurate. Due to the substantial difficulties of the measurement technique in the blowing region (probing by the LDV method in the area of multiple, discrete jets exhausting air out from the cavity) the resulting experimental points constitute a rather crude estimation of the real distribution. Still, the intensity of blowing is captured correctly ($U_{\mathrm{t}} < 5.5\,\mathrm{m\,s^{-1}}$). The areas of $U_{\mathrm{t}} > 0\,\mathrm{m\,s^{-1}}$ and $U_{\mathrm{t}} < 0\,\mathrm{m\,s^{-1}}$ are unequal, but the the net mass flow rate is kept constantly at $0\,\mathrm{kg\,s^{-1}}$ thanks to a natural adaptation of the streamwise variation of the transpiration intensity. The obtained correlation suggests that the aerodynamic porosity value of the plate p_{aero} (unknown) is not far from the nominal porosity $p_{\mathrm{nom}} = 5.7\%$ used as an input to the numerical model. It was suspected that in a real flow a transition of the transpiration velocity value, from $0\,\mathrm{m\,s^{-1}}$ at the impermeable wall immediately up to a maximum value of U_{t} at the ventilated surface fore and aft edges, is smooth. Therefore, the blending (buffer) zones were introduced, interchanging a sudden increase of U_{t} with a more gradual, linear variation over the distance of 5 mm (see Figure 8). This modification improves the coincidence of the experimental and CFD results, especially regarding the position and angle of the front, oblique shock wave of the λ-foot structure.

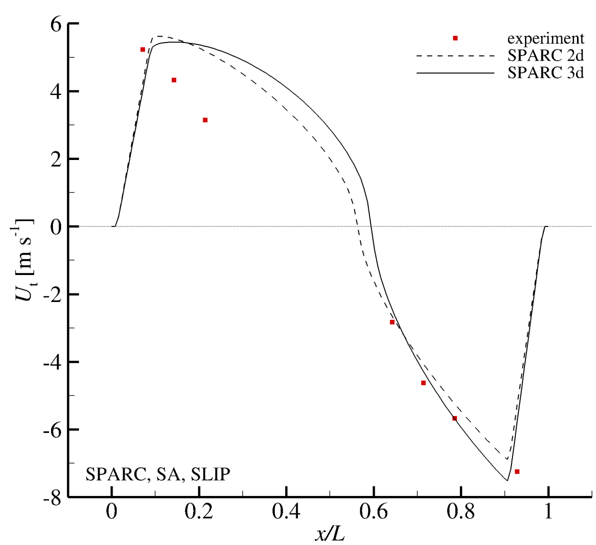

Figure 8: Transpiration velocity U_{t} distribution over the perforated wall

The passive control system has a large influence on the boundary layer development along the channel lower wall, which is demonstrated in Figure 9 for the streamwise velocity component U_x/U_{ref}. Three cross-sections (marked in Figures 6 and 7) are displayed: $x_1 = 115\,\mathrm{mm}$ (15 mm upstream of the forward edge of the cavity), $x_2 = 140\,\mathrm{mm}$ (between the front, oblique and the rear, normal shocks), and $x_3 = 190\,\mathrm{mm}$ (10 mm before the rear edge of the perforated plate). The fit of the experimental and numerical profiles is remarkable, confirming the importance of the three-dimensional model preparation. The incoming, reference boundary layer shape ($x_1 = 115\,\mathrm{mm}$), being independent of the presence of the transpiration flow, is well replicated for both 2d and 3d simulations, which is an essential requirement of the subsequent interaction and ventilation analysis. Between the front and rear compressions ($x_2 = 140\,\mathrm{mm}$) the reference profile is still almost unaffected by the interaction process taking place more downstream. At the same cross-section the transition through the generated oblique shock is present, noticeable as a kink in the velocity profile subjected to flow control (at a distance of 15 mm from the surface), which is fully captured by both calculations (2d and 3d). Only downstream of the rear leg of the λ-foot structure ($x_3 = 190\,\mathrm{mm}$) the air velocity becomes fully subsonic. The profile subjected to ventilation is more disturbed (less filled), indicating even a presence of a flat separation region of 0.6 mm height. Moreover, a higher value of U_x/U_{ref} above the viscous region is a consequence of a decreased effective cross-section area of the tunnel due to a more intensive thickening of the boundary layers destabilised by the upstream blowing from the cavity volume. The 3d solutions are still fitting the test data very satisfactorily, resolving even the extent of the described reversed flow. Only the presented 2d results reveal a growing deformation of the velocity profile that builds-up a discrepancy with the experimental points with increasing distance from the investigated shock system.

Figure 10 presents turbulent (Reynolds) shear stress $R_{xy}^{\mathrm{turb}}/\rho\,U_{\mathrm{ref}}^2$ profiles at three chosen cross-sections: $x = 115\,\mathrm{mm}$, 140 mm, and 190 mm. Again, the incoming, reference profile ($x_1 = 115\,\mathrm{mm}$) is independent of the presence of the transpiration flow. Unfortunately, due to an insufficient accuracy of the LDV method in the near-wall zone the peak of $R_{xy}^{\mathrm{turb}}/\rho\,U_{\mathrm{ref}}^2$ (located at $y < 0.1\,\mathrm{mm}$) could not be captured. The calculated shear stresses (equal in 2d and 3d) seem to fit acceptably the experimental points, with a slight shift towards the higher values. As before, at the following position of $x_2 = 140\,\mathrm{mm}$ the reference profile is almost unaffected by the interaction process taking place more downstream. Still, the maximum of $R_{xy}^{\mathrm{turb}}/\rho\,U_{\mathrm{ref}}^2$ is not recorded by LDV. In contrast, when the passive control system is activated a large increase of the turbulence intensity is observed, with the extremum clearly visible farther away from the surface. The general agreement with the numerical results is acceptable, with the 2d and 3d solutions being almost indistinguishable from each other. The most significant discrepancies between the two- and three-dimensional modelling is no-

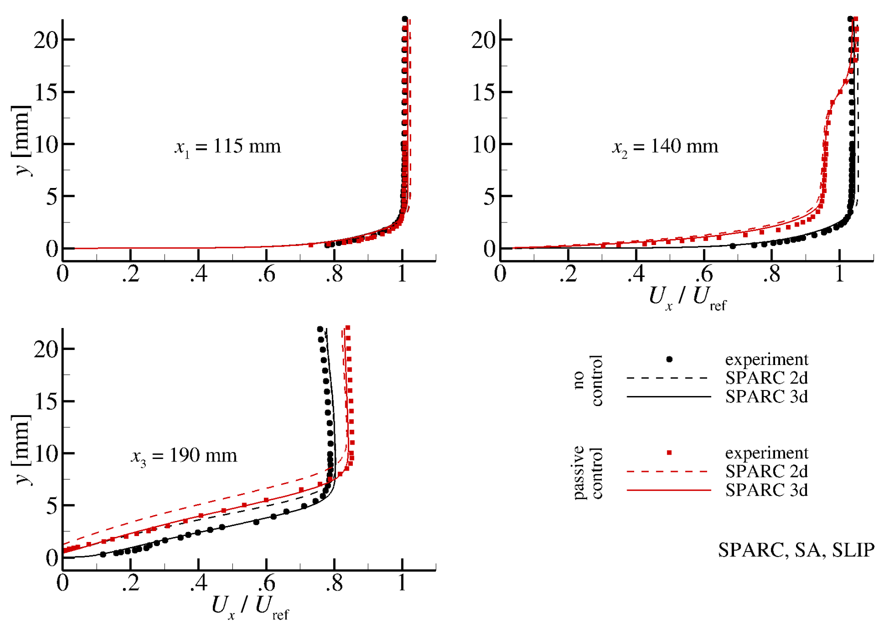

Figure 9: Streamwise velocity U_x/U_{ref} profile at $x = 115\,\mathrm{mm}$, 140 mm, and 190 mm

ticeable downstream of the interaction region ($x_3 = 190\,\mathrm{mm}$). Here the 3d predictions almost exactly match the experimental data for both investigated configurations (reference and with flow control). A considerable scatter of the points near the peak value of the Reynolds shear stress (increased because of ventilation) is a consequence of high measurement errors. The 2d computations indicate higher values of $R_{xy}^{\mathrm{turb}}/\rho\, U_{\mathrm{ref}}^2$ (not confirmed by the wind tunnel survey) with the maxima moved farther away from the wall.

The boundary layer thickness δ estimation relies on a simplified approach often employed for a viscous, compressible zone analysis in the flat-plate flow. A drop of the stagnation pressure p_0 over the shocks and a presence of the static pressure p gradient in the direction normal to the wall are neglected. Additionally, due to a lack of the measurement of $p\,(y)$ in the vertical traverses the available wall values p_{w} are extrapolated from the surface to the main stream, i.e.: $p\,(y) = p_{\mathrm{w}} = \mathrm{const}$. Under such assumptions the ideal velocity profile U_x^{i} is fixed and equal to the maximum value of the real velocity profile $U_x(y)$ in the core, just above the boundary layer, i.e. $U_x^{\mathrm{i}} = U_x(y \gg \delta) = \mathrm{const}$ (see the reference profiles in Figure 9). The thickness δ is defined as a distance from the wall y at which the real profile $U_x(y)$ is reaching 99.5% of the ideal profile U_x^{i}. The condition of constant stagnation temperature T_0 in the flow-field (equal to the value of 300 K measured at the inlet) together with Equations (1) for $T(y)$ allow for a calculation of the density profile $\rho\,(y)$, the boundary layer displacement δ^* and momentum θ thicknesses, as well as the compressible shape factor H:

$$\rho\,(y) = \frac{p_{\mathrm{w}}}{R\,T(y)} \ , \quad \delta^* = \int_0^{\delta} \left[1 - \frac{\rho\,(y)\,U_x(y)}{\rho^{\mathrm{i}}\,U_x^{\mathrm{i}}}\right] dy \ , \quad \theta = \int_0^{\delta} \frac{\rho\,(y)\,U_x(y)}{\rho^{\mathrm{i}}\,U_x^{\mathrm{i}}} \left[1 - \frac{U_x(y)}{U_x^{\mathrm{i}}}\right] dy \ , \quad H = \frac{\delta^*}{\theta} \ . \qquad (2)$$

For the flat plate flow the ideal density profile ρ^{i} appearing in Equations (2) is constant (analogously to U_x^{i}), i.e. $\rho^{\mathrm{i}} = \rho\,(y \gg \delta) = \mathrm{const}$. What important, in the post-processing of the wind tunnel and computational velocity profiles exactly the same numerical procedure is utilized for determination of the boundary layer edge δ and parameters: δ^*, θ, and H. The cohesion of the algorithm turns out to be a necessary requirement of the analysis aiming at obtaining an acceptable correlation between the experimental and CFD data.

A streamwise development of the boundary layer thickness δ and the integral parameters: displacement thickness δ^*, momentum thickness θ, and compressible shape factor H is demonstrated in Figure 11. Only the LDV measurement window is considered ($115\,\mathrm{mm} < x < 260\,\mathrm{mm}$) and displayed. For the reference configuration the thickness δ remains approximately constant (4 mm) up to a location where a sudden increase of pressure appears induced by a presence of the front compression of the λ-foot structure ($x = 150\,\mathrm{mm}$) preceding the main shock wave. The activation of the passive control system leads to a severe destabilisation of the velocity profile $U_x(y)$ due to the blowing from the upstream part of the cavity ($130\,\mathrm{mm} < x < 170\,\mathrm{mm}$).

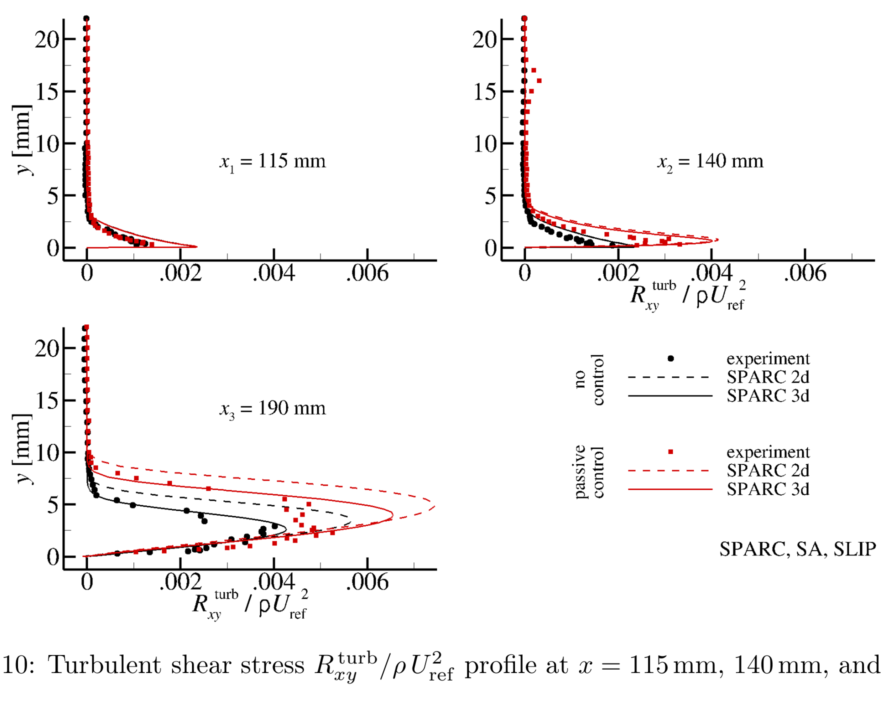

Figure 10: Turbulent shear stress $R_{xy}^{\mathrm{turb}}/\rho\, U_{\mathrm{ref}}^2$ profile at $x = 115\,\mathrm{mm}$, 140 mm, and 190 mm

The suction downstream ($170\,\mathrm{mm} < x < 200\,\mathrm{mm}$) is not sufficiently effective to bring its shape back to the reference level. The growth of the ventilated boundary layer thickness is higher by 4 mm (by 38%) compared to the uncontrolled case. The numerical results agree reasonably well with the experimental data, especially in the incoming stream and in the interaction region itself ($115\,\mathrm{mm} < x < 200\,\mathrm{mm}$). Downstream of the cavity ($x > 200\,\mathrm{mm}$) the 2d and 3d solutions start to diverge more noticeably. The displacement thickness δ^* is a better measure of the deformation of the velocity profile $U_x(y)$. The wind tunnel data indicate an increase of the ratio of the global maximum δ^*_{max} to the reference value δ^*_{ref} in the incoming stream from $\delta^*_{\mathrm{max}}/\delta^*_{\mathrm{ref}} = 5.6$ up to $\delta^*_{\mathrm{max}}/\delta^*_{\mathrm{ref}} = 9.6$ (by 71%) in controlled conditions. The computations predict a worsening of the state of the boundary layer as well, resulting in a rise of the $\delta^*_{\mathrm{max}}/\delta^*_{\mathrm{ref}}$ value in 2d from 6.7 to 9.7 (by 45%) and in 3d from 4.5 to 7.5 (by 67%). The agreement between the three-dimensional simulations and the experimental points is satisfactory, particularly upstream of the rear edge of the cavity. Finally, in case of the momentum thickness θ the presence of the transpiration flow forces a rise of the ratio of the global maximum θ_{max} to the reference value θ_{ref} in the incoming stream $\theta_{\mathrm{max}}/\theta_{\mathrm{ref}}$ from 7.0 up to 10.0 (by 43%). Again, the computational curves acceptably match the test data, notably for $x < 200\,\mathrm{mm}$, suggesting a growth in 2d from 5.0 to 6.7 (by 34%) and in 3d from 4.0 to 5.7 (by 43%). The visible increase of the compressible shape factor H is a consequence of the reduction of the velocity profile fullness which manifests itself directly through a weakened resistance of the boundary layer to flow separation. At the inlet to the interaction zone ($x = 115\,\mathrm{mm}$) the measured value of H is equal to 2.5. In the reference conditions the action of the normal shock wave forces a rise of the shape factor up to 3.1 (by 24%). When the passive control system is activated a more pronounced increment of H (up to 4.3, by 39%) is observed. Downstream of the extrema ($x > 200\,\mathrm{mm}$) the disturbed profiles are subjected to a regeneration, reaching $H = 1.9$ (reference) and $H = 2.2$ (passive ventilation). Both numerical models (2d and 3d) indicate the same shape factor of 2.2 at $x = 115\,\mathrm{mm}$. The agreement of the three-dimensional solutions with the LDV measurements is remarkable in the entire investigated region. The numerical analysis suggests the following extrema of H: 4.6 and 5.5 (in 2d) and 3.5 and 4.3 (in 3d) above the impermeable and perforated walls respectively.

The passive control of the shock wave–boundary layer interaction in the transonic nozzle with a flat wall (ONERA) has already been investigated numerically in the past using RANS solvers: NASCA (2d, 0- and 2-equation closures, BD and Poll–Danks–Humphreys (PDH) models [9]) and FLU3M (2d and 3d, 2-equation and RSM closures, Darcy, BD, and PDH models [10]). The presented SPARC solutions (SA and BD) obtained using relatively dense 3d grids proved to be more accurate compared to the predictions published in the cited papers. Moreover, the level of agreement between the experimental and CFD results is similar for the reference as for the flow control case, which was the main goal of the validation process.

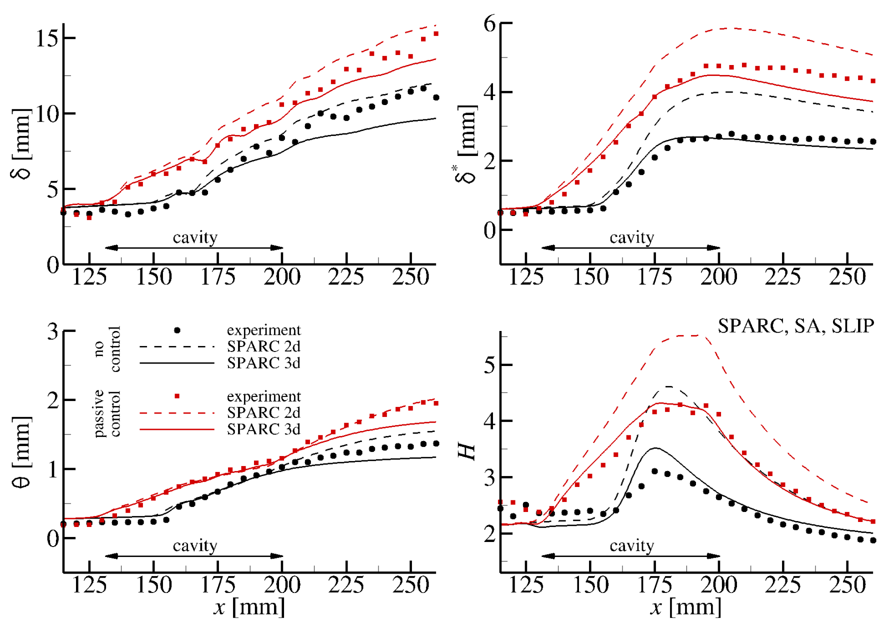

Figure 11: Boundary layer thickness δ, displacement δ^* and momentum θ thicknesses, and shape factor H

5 Curved Duct with Local Supersonic Area

The second studied test case is a quasi-two-dimensional flow in the curved duct (investigated experimentally by W. Braun in the transonic wind tunnel of the University of Karlsruhe in Germany [5]) with the interaction process taking place on the convex, lower wall (Figure 12). It was equipped with a 71 mm (72 mm in terms of the arc length s) cavity covered by a 1.5 mm thick perforated plate (marked as number 2 and referenced to as 0/72) of nominal porosity $p_{\mathrm{nom}} = 8.2\%$ (3400 normal, conical in shape holes of a diameter of 0.3 mm and 0.4 mm at the main flow and cavity sides respectively). The test section width (distance between the side walls) was 50 mm. The Mach–Zehnder interferometer delivered the visualizations of the shock wave topology. Pressure was measured at the lower wall (p), in the symmetry plane of the channel and at the bottom of the cavity (p_{c}). The static and stagnation pressure values were surveyed by pneumatic probes in three vertical traverses: $s_1 = 32$ mm, $s_2 = 68$ mm, and $s_3 = 80$ mm. Such detailed data allowed for a determination of the velocity profiles, and hence for a calculation of the boundary layer integral parameters: δ^*, θ, and H at the given locations. The stagnation values of pressure p_0 and temperature T_0 of air entering the test section were equal to: $p_0 = 92\,700$ Pa, $T_0 = 284$ K (reference) and $p_0 = 91\,730$ Pa, $T_0 = 290$ K (passive control). The turbulence level at the inlet was unknown. A normal shock wave (terminating a local supersonic area) with the shock upstream isentropic Mach number of $Ma_{\mathrm{is}} = 1.32$ was positioned above the cavity centre. The incoming turbulent boundary layer thickness δ just upstream of the interaction zone was approx. 3 mm.

The computational domain consisted of the central part of the test section alone, modelling of the inlet was not necessary (Figure 13). Instead of the regulated throat a prolongation of the channel walls was applied, allowing for a convenient positioning of the shock wave in the duct (by setting the outlet pressure only). The opening angle was determined (through calibrating simulations) in such a way to ensure (in the 3d reference case) the same position of the shock and upstream Mach number value as were present in the wind tunnel. Only one half of the channel was modelled in 3d utilizing the symmetry boundary condition, therefore the distance between the side wall and the symmetry plane was 25 mm, equal to 50% of the duct width 50 mm. The shock upstream isentropic Mach number $Ma_{\mathrm{is}} = 1.32$ did not lead to a development of a significant flow separation zone. The origin of the coordinate system was positioned atop of the arc of the radius $R = 300$ mm ($x = 0$ mm), while the cavity covered by a perforated plate was located between $x = 0$ mm ($s = 0$ mm) and $x = 71$ mm ($s = 72$ mm). The secondary flows intensification and eruption of corner separation problem did not appear, possibly due to a strong acceleration of the flow in the curved channel.

A base 3d mesh with standard resolution of $169 \times 129 \times 65$ ($1.4 \cdot 10^6$ volumes) was modified by a local grid refinement (8 times) of block 2, containing the shock wave–boundary layer interaction and wall ventilation regions (highlighted in red colour in Figure 13), and designated $169 \times 129 \times 65+$ ($5.1 \cdot 10^6$ volumes). For comparison purposes a globally refined (8 times) mesh $337 \times 257 \times 129$ ($11.0 \cdot 10^6$ volumes) was generated. A 2d grid $169 \times 129+$ was created through an extraction of the symmetry plane from the 3d model $169 \times 129 \times 65+$. The vertical size of the first layer of cells in the near-wall region was set to $\Delta y \leq 2 \cdot 10^{-6}$ m

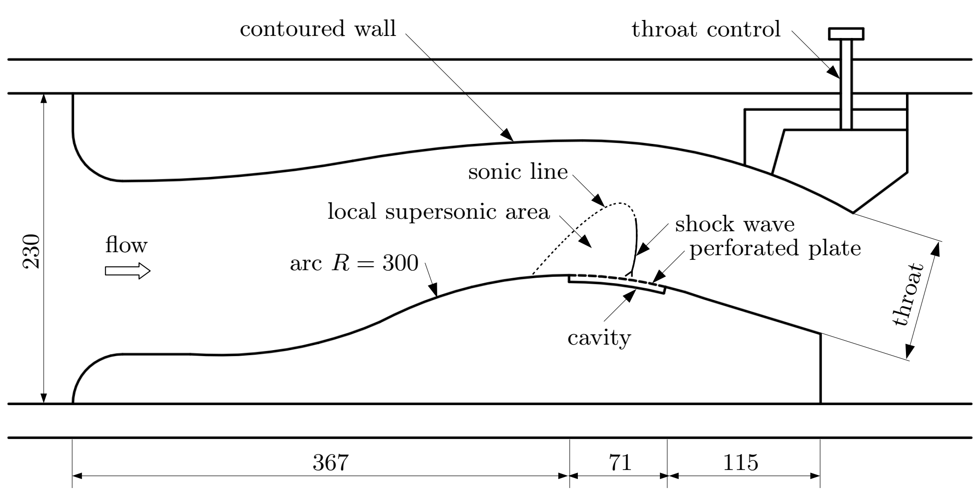

Figure 12: Curved duct with local supersonic area (University of Karlsruhe)

($y^+ \ll 1$). At the channel inlet the stagnation parameters boundary condition was applied with total pressure and total temperature equal to: $p_0 = 92\,700\,\mathrm{Pa}$, $T_0 = 284\,\mathrm{K}$ (reference) and $p_0 = 91\,730\,\mathrm{Pa}$, $T_0 = 290\,\mathrm{K}$ (flow control), together with two flow angles $\alpha = \beta = 0°$, and the eddy viscosity ratio $\mu_{\mathrm{turb}}/\mu_{\mathrm{lam}} = 1$. Due to an absence of the regulated throat in the computational model the position of the shock was determined by the pressure ratio p/p_0 value at the outlet, i.e. 0.656 in 2d and 0.568 in 3d. For three external solid walls (no-slip) the impermeable and adiabatic surface boundary condition was applied, interchanged with the perforated (permeable) wall boundary condition (nominal porosity $p_{\mathrm{nom}} = 8.3\%$) in the passive control region. The effective (aerodynamic) porosity p_{aero} was estimated (9.1% for blowing and 8.2% for suction) based on a set of mass flow rate measurements conducted in Karlsruhe prior to the main investigations of the interaction phenomenon. The temperature in the cavity T_{c} was kept constant at 290 K. The convergence criteria was based on a 5 orders of magnitude reduction of the density residual, accompanied by a stabilisation of the aerodynamic forces acting on the walls and, in case of the passive control, of the cavity pressure p_{c}. The grid dependency study (adopting a solution of the reference flow), based on the comparison of wall pressure and friction coefficient distributions, proved that the locally refined grid $169 \times 129 \times 65+$ delivered accuracy of the globally refined mesh $337 \times 257 \times 129$ with half the number of cells.

Experimental interferograms (depicted in Figure 14) present the effect of the "extended" passive control on the flow structure. The reference case corresponds to a normal shock wave–turbulent boundary layer interaction phenomenon at a moderate isentropic Mach number $Ma_{\mathrm{is}} = 1.32$ (Figure 14a). Near the lower, convex wall a local supersonic area develops terminated by a shock wave of a decreasing intensity with the distance from the surface – a typical flow configuration often found on a transonic airfoil or a helicopter main rotor blade. The beginning of the formation of a small λ-foot is noticeable near the wall. The shock induced pressure rise is not sufficient to cause separation which occurs in the curved duct for higher Mach numbers $Ma_{\mathrm{is}} > 1.35$. The upstream blowing from the cavity into the main stream (taking place from $x/L = 0$ to $x/L = 0.8$) highly disturbs the incoming boundary layer (Figure 14b). A strong, normal shock wave is interchanged with a system of weaker, oblique compression and expansion waves reflecting between the wall and the edge of the supersonic region, which reduces the maximum Mach number to $Ma_{\mathrm{is}} = 1.17$. This drop is a consequence of the upstream shift of the initial compression to the forward edge of the perforated plate. The suction present in the downstream 20% of the perforated plate is not strong enough to counteract the negative disturbance introduced by the upstream blowing. It cannot neither bring the boundary layer to the initial state nor counteract the appearing separation. The transformation of a strong, normal shock into a system of weaker, oblique disturbances ensures an almost complete elimination of the wave

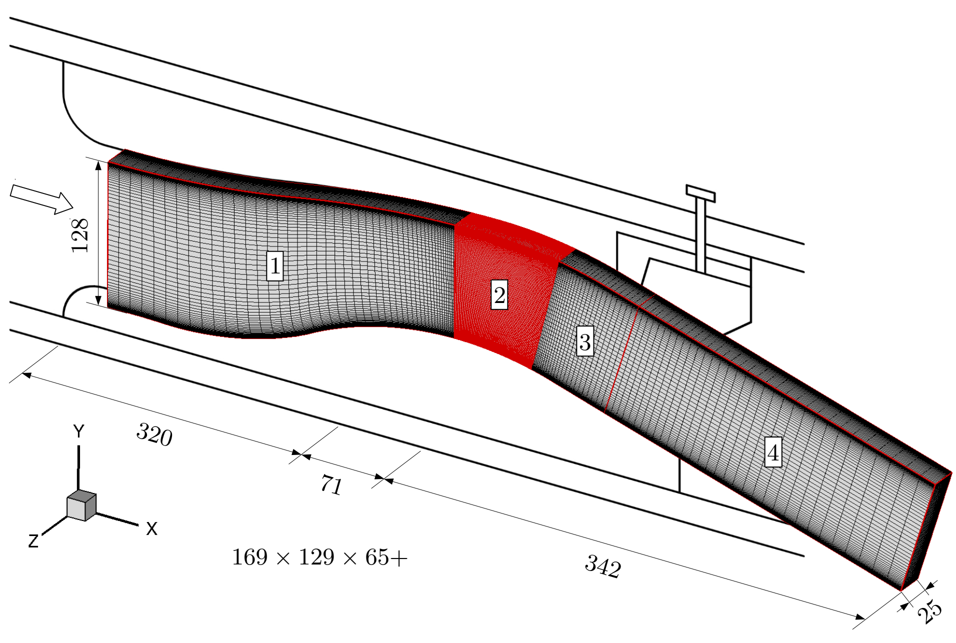

Figure 13: Numerical mesh $169 \times 129 \times 65+$ ($5.1 \cdot 10^6$ of control volumes)

losses. Unfortunately, it is accompanied by a significantly more pronounced thickening of the boundary layer and growth of the viscous losses, compared to the "classical" version of the passive control arrangement.

Figure 14 contains numerical counterparts of the discussed interferograms in a form of the density ρ isolines (fringe patterns) in the symmetry plane of the curved channel. The visualisations of 2d and 3d results faithfully replicate the experimental topology transformation. Lack of side walls in the 2d model results in a higher expansion of the reference flow ($Ma_{\mathrm{is}} = 1.37$), which is the main reason of a larger λ-foot size and a more severe destabilization of the boundary layer downstream of the interaction region compared to the 3d solution ($Ma_{\mathrm{is}} = 1.33$). Due to the appearance of transpiration the normal shock wave is interchanged with a system of weaker, oblique compressions and expansions, which reduces flow losses related to a sudden drop of velocity from a supersonic to subsonic value. In parallel, the shock upstream isentropic Mach number is limited to $Ma_{\mathrm{is}} = 1.18$ in 2d and $Ma_{\mathrm{is}} = 1.17$ in 3d. The disturbing action of the bleeding significantly weakens the shear stress at the wall, reducing the tangential component of the aerodynamic force due to friction. Figure 14b presents also the transpiration velocity U_{t} distributions which are characterised by a presence of a long zone ($0 < x/L < 0.8$) of moderate blowing ($U_{\mathrm{t}} < 7\,\mathrm{m\,s^{-1}}$), terminated ($0.8 < x/L < 1.0$) by a localised, intensive suction ($U_{\mathrm{t}} < 15\,\mathrm{m\,s^{-1}}$). In relation to the full, three-dimensional analysis the 2d modelling predicts only slightly higher values of U_{t} for both ventilation directions.

The flow recirculation through the cavity, in the opposite direction to the main flow, forces a flattening of the bottom wall pressure p/p_0 distribution in the whole interaction region (Figure 15). The presented solutions are obtained with the help of blending (buffer) zones of 5 mm length placed at the front and rear extremities of the perforated plate. The pressure in the cavity p_{c} is stabilising naturally, ensuring a zero net mass-flux through the ventilated surface at any given time. It is assumed that the unknown temperature

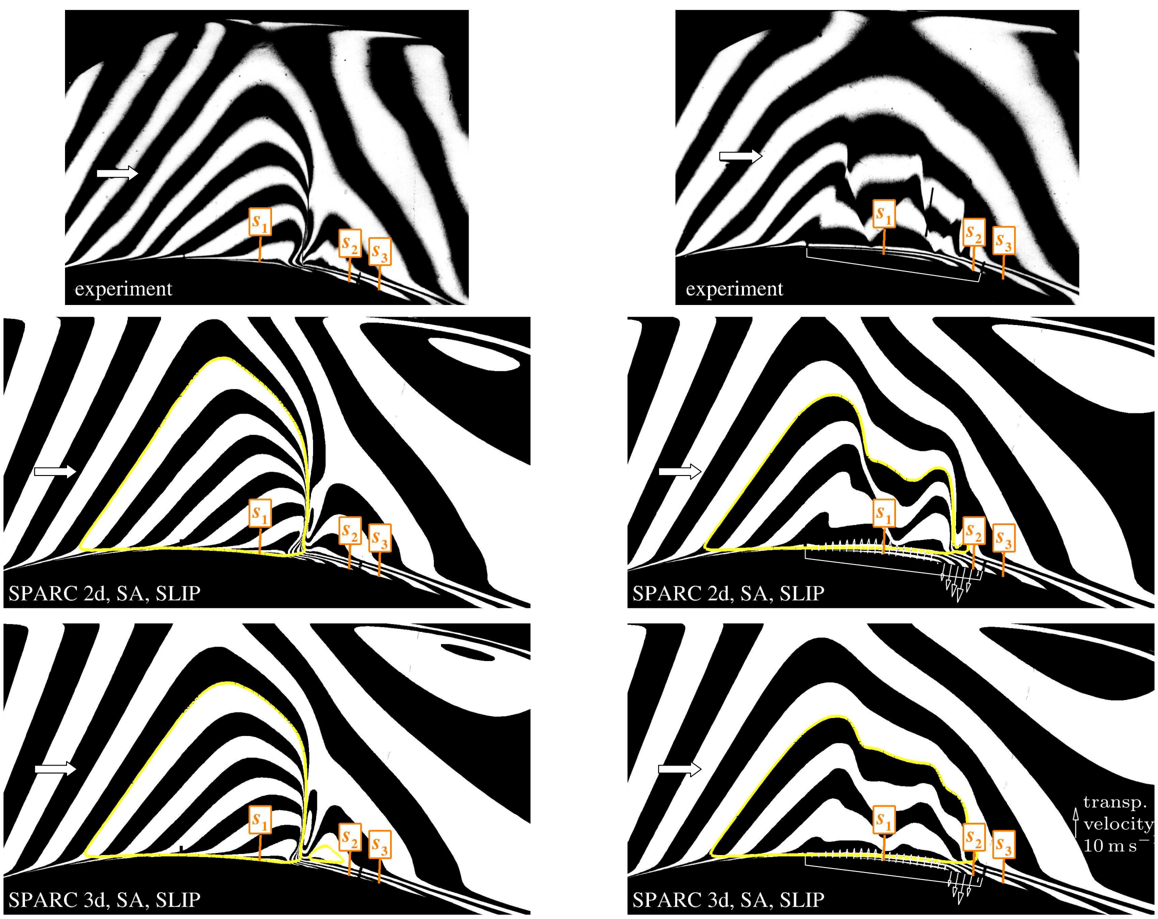

(a) reference (b) passive control

Figure 14: Experimental interferograms and 2d/3d CFD solutions ($Ma_{\mathrm{is}} = 1.32$)

in the cavity T_c is constant and equal to the stagnation temperature at the inlet $T_0 = 290\,\mathrm{K}$. The results of 3d simulations agree well with the measurements upstream ($x < 0\,\mathrm{mm}$) of the shock system and just above the cavity position ($0\,\mathrm{mm} < x < 71\,\mathrm{mm}$). Downstream of the passive control system ($x > 71\,\mathrm{mm}$) a slight discrepancy exist. In case of the two-dimensional results not only the pressure is much lower before the interaction, but also a too high downstream level is predicted in comparison with the test points, emphasizing the impact of the side-wall boundary layers on the flow development in the duct. The measured value of pressure in the cavity system $p_c/p_0 = 0.444$ is captured numerically ($p_c/p_0 = 0.435$), with a deviation reaching approx. 2% regardless of the choice of the computational model (2d or 3d). In case of the controlled flow modelled in the full, three-dimensional geometry of the channel the lack of buffer zones shifts the location of the initial oblique compression by 5 mm upstream which seems now to start too early regarding the recorded wall pressure p/p_0 distribution. Additionally, as a verification the cavity volume was divided into multiple streamwise sections. The resultant flow parameters were identical as in case of a single cavity volume, which acknowledged a negligible level of the cross-wise recirculation in the cavity. Taking into account the stabilisation process of the temperature in the cavity T_c resulted in a value that is only 5 K lower than the stagnation temperature at the inlet $T_0 = 290\,\mathrm{K}$, which sanctions the initial assumption. These findings are similar to the conclusions drawn during the analysis of the flow in the nozzle with a flat wall (Section 4).

Due to a variation of the inlet stagnation parameters for the reference and flow control configurations instead of the tangential velocity component the Mach number *Ma* profiles are presented in Figure 16. The experimental and numerical values are calculated out of the data extracted in the vertical direction (in three traverses: s_1, s_2, and s_3 – see Figure 14), in line with the translation of the pneumatic probes in the wind tunnel. The static $p(y)$ and total $p_0(y)$ pressure profiles allow for a determination of the Mach number *Ma*:

$$Ma = \sqrt{\frac{2}{\gamma-1}\left\{\left[\frac{p(y)}{p_0(y)}\right]^{\frac{\gamma}{\gamma-1}} - 1\right\}}\,. \tag{3}$$

The traverse s_1 is located in the supersonic area, 32 mm downstream of the cavity forward edge ($s = 0\,\mathrm{mm}$), in a zone subjected to moderate blowing when the surface ventilation is active. The traverse $s_2 = 68\,\mathrm{mm}$ is positioned in a region of strong suction, 4 mm upstream of the cavity rearward edge ($s = 72\,\mathrm{mm}$). Finally, the traverse $s_3 = 80\,\mathrm{mm}$ is situated above the impermeable wall, 8 mm downstream of the passive control

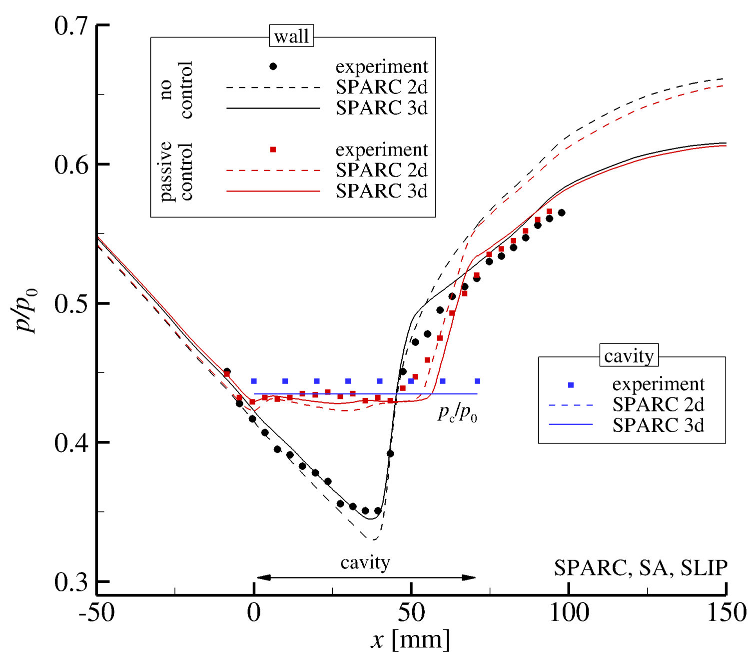

Figure 15: Bottom wall pressure p/p_0 distribution

system. Due to a presence of the transverse pressure gradient near the lower, convex wall of the duct the reference Mach number profile in s_1 (upstream of a normal shock wave) exhibits a typical behaviour with decreasing values of Ma with increasing distance y from the surface. In passive control conditions s_1 is located behind a system of three waves, generating a total pressure drop, and hence a retardation of the flow. In the traverse $s_2 = 68\,\mathrm{mm}$ a similar behaviour is observed, but only below the boundary layer edge. Above the area dominated by viscous effects ($y > 5\,\mathrm{mm}$) the stagnation pressure losses are lower (therefore Ma is higher) when the air passes through a system of weaker, oblique waves compared to a single, normal shock wave. Beyond the interaction region (s_3) the positive influence of ventilation disappears, leaving behind a large deficit of velocity resulting from a more severe destabilisation of the boundary layer. It can be noticed in the figure that in the regions of a reversed flow it is assumed that $Ma = 0$ – a straightforward consequence of the employed measurement technique. For the reference case the experimental data does not indicate any presence of separation in: s_1, s_2, and s_3. On the contrary, when blowing and suction through perforation are present, a flat reversed flow area (of 0.5 mm height) is visible in s_2 and s_3 profiles.

The numerical Mach number Ma profiles (reference case) satisfactorily fit the experimental data in all three traverses, upstream (s_1) and downstream (s_2 and s_3) of the normal shock wave. A noticeable in s_1 difference between the curves derived from 2d and 3d results is augmented by the interaction process (s_2 and s_3). It proves that the boundary layer development in the curved channel cannot be properly captured using a simplified two-dimensional computational model. A qualitative impact of the ventilation process on the evolution of the Ma number profiles is predicted correctly. In all locations (s_1, s_2, and s_3) the amplified viscous losses of the stagnation pressure due to passive control cause the velocity to be lower below the boundary layer edge. On the contrary, downstream of the shock structure (s_2 and s_3) this character is opposite in the main stream, since a single, normal compression induces larger wave losses compared to a system of much weaker, oblique waves. The visible disagreements are probably the effect of a lack of the separation zone (of 0.5 mm height) present in the measurements in s_2 and s_3. Because the flow around the local supersonic area is subsonic in nature, such a discrepancy may affect the flow-field upstream of the interaction region (s_1).

The estimation of the boundary layer development in the curved duct is based on the experimental static $p\,(y)$ and total $p_0(y)$ pressure profiles measured in three vertical traverses: s_1, s_2, and s_3. The velocity profile $U(y)$ is derived from Equation (3) and employing the definition of Mach number $Ma(y)$:

$$U(y) = Ma(y)\,\sqrt{\gamma\, R\, T(y)}\ . \tag{4}$$

The condition of constant stagnation temperature T_0 in the whole flow-field (equal to the value measured

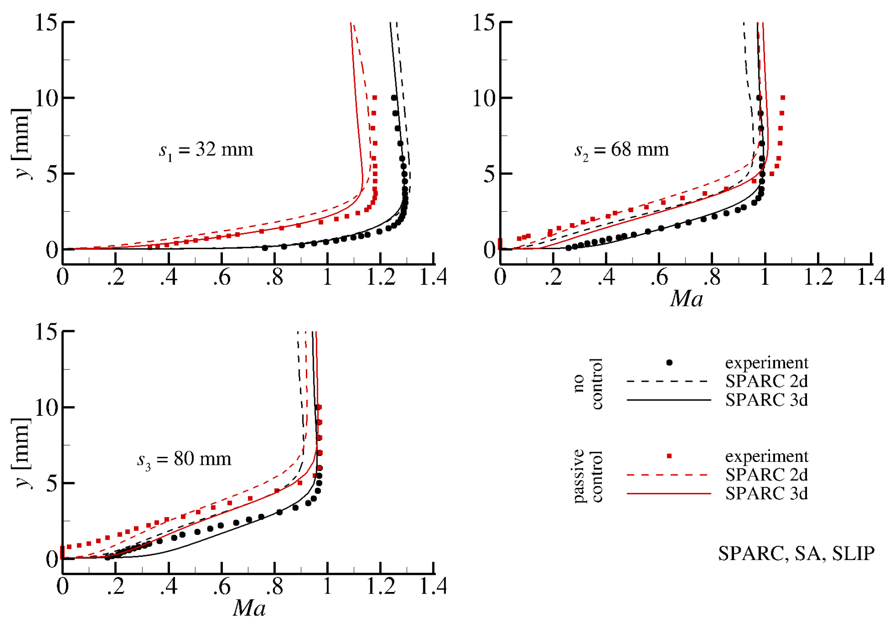

Figure 16: Mach number Ma profile at $s = 32\,\mathrm{mm}$, 68 mm, and 80 mm

at the channel inlet) allows for a determination of the temperature $T(y)$ and density $\rho\,(y)$ profiles:

$$T(y) = T_0 \left\{ 1 + \frac{\gamma - 1}{2} \left[Ma(y) \right]^2 \right\}^{-1} \quad , \quad \rho\,(y) = \frac{p\,(y)}{R\,T(y)} \quad . \tag{5}$$

The theoretical (ideal) profiles of velocity $U^{\,\mathrm{i}}(y)$ and density $\rho^{\,\mathrm{i}}(y)$ are directly calculated from Equations: (3), (4), and (5) when no stagnation pressure losses are assumed, i.e. $p_0 = p_0(y \gg \delta) = \mathrm{const.}$ In presence of a transverse pressure gradient the thickness δ is defined as a distance from the wall y at which the real profile $U(y)$ is reaching 99.5% of the ideal profile $U^{\,\mathrm{i}}(y)$. The boundary layer integral parameters: displacement δ^* and momentum θ thicknesses, as well as the compressible shape factor H are defined by:

$$\delta^* = \int_0^{\delta} \left[\frac{\rho^{\,\mathrm{i}}(y)\,U^{\,\mathrm{i}}(y) - \rho\,(y)\,U(y)}{\rho^{\,\mathrm{i}}(0)\,U^{\,\mathrm{i}}(0)} \right] dy \quad , \quad \theta = \int_0^{\delta} \left\{ \frac{\rho^{\,\mathrm{i}}(y)\,\left[U^{\,\mathrm{i}}(y)\right]^2 - \rho\,(y)\,\left[U(y)\right]^2}{\rho^{\,\mathrm{i}}(0)\,\left[U^{\,\mathrm{i}}(0)\right]^2} \right\} dy - \delta^* \quad , \quad H = \frac{\delta^*}{\theta} \quad . \tag{6}$$

A streamwise development of the boundary layer thickness δ and the integral parameters: displacement thickness δ^*, momentum thickness θ, and compressible shape factor H is depicted in Figure 17. For the reference configuration the thickness δ remains approximately constant (3 mm) up to a position where a sudden growth of pressure appears induced by a presence of the front, oblique compression of the λ-foot structure ($x = 40\,\mathrm{mm}$) preceding the main, normal shock wave. The activation of the passive control system leads to a major destabilisation of the velocity profile $U(y)$ due to the mild blowing from the upstream 80% of the cavity length ($0\,\mathrm{mm} < x < 55\,\mathrm{mm}$). The suction downstream ($55\,\mathrm{mm} < x < 71\,\mathrm{mm}$) is not sufficiently powerful to bring its shape back to the initial level. The growth of the ventilated boundary layer thickness is higher by 2.3 mm (by 22%) compared to the uncontrolled case. The numerical results agree acceptably well with the experimental data available in traverses: s_1, s_2, and s_3. The largest deviations between the 2d and 3d solutions exist above the cavity location ($0\,\mathrm{mm} < x < 71\,\mathrm{mm}$), with the difference vanishing on both sides of this range. The numerical data indicate an increase of the ratio of the global maximum of displacement thickness δ^*_{max} to the reference value δ^*_{ref} in the incoming stream $\delta^*_{\mathrm{max}}/\delta^*_{\mathrm{ref}}$ from 7.6 up to 10.1 in 2d (by 33%) and from 8.4 up to 11.6 in 3d (by 38%) in controlled conditions. The two-dimensional model predicts a too large rise of δ^* on the shock system, compared to the three dimensional solutions which reveal a more acceptable level of agreement with the wind tunnel data. A visible discrepancy between the CFD

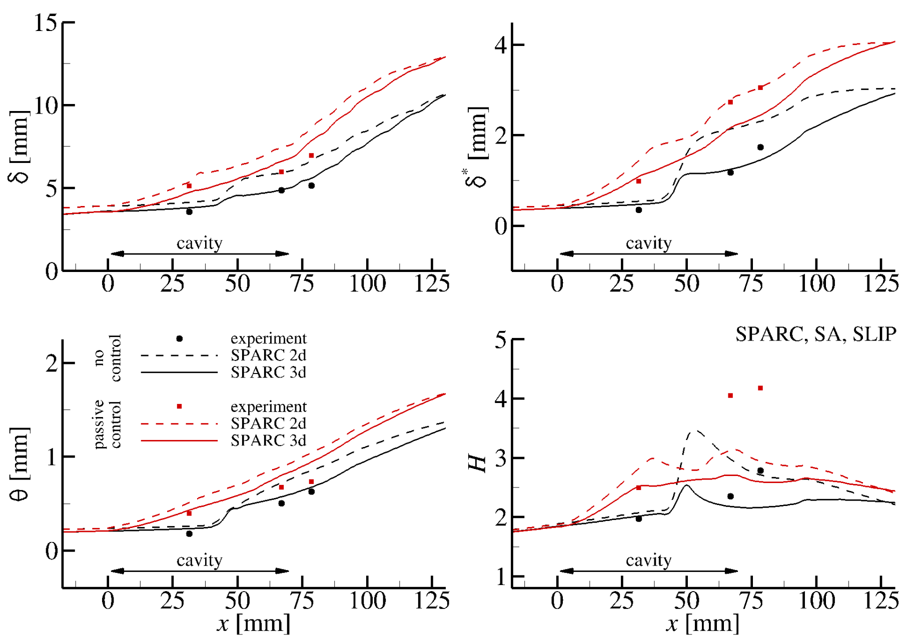

Figure 17: Boundary layer thickness δ, displacement δ^* and momentum θ thicknesses, and shape factor H

and the experimental values obtained at locations s_2 and s_3 (passive venting) is a consequence of the inability of the computational model to capture a small separation zone noticeable in the Mach number profiles of Figure 16. For the momentum thickness θ the presence of the transpiration flow forces a rise of the ratio of the global maximum θ_{max} to the reference value θ_{ref} in the incoming stream $\theta_{\mathrm{max}}/\theta_{\mathrm{ref}}$ from 6.1 up to 7.4 in 2d (by 21%) and from 6.6 up to 8.5 in 3d (by 29%). Again, the computational curves satisfactorily match the test data in traverses: s_1, s_2, and s_3. In the reference conditions the measured value of the shape factor H at the inlet to the interaction zone (s_1) is equal to 2.0. The action of the normal shock wave forces a rise of H up to $2.4 - 2.8$ (s_2 and s_3). When the passive control system is activated the velocity profiles become less filled, and a more pronounced increment of H (up to 2.5, 4.1, and 4.2 in s_1, s_2, and s_3 respectively) is observed. Regardless of the employed approach (2d or 3d) the same level of $H = 1.8$ is found for the undisturbed, upstream boundary layer ($x = -10\,\mathrm{mm}$). In location s_1 the computed shape factor values: 2.1 (2d, reference), 2.0 (3d, reference), 2.8 (2d, flow control), and 2.5 (3d, flow control) match the measurement points very well (particularly in 3d). In locations s_2 and s_3 this comparison is still acceptable for the reference configurations indicating: 3.0 and 2.7 (in 2d) and 2.2 and 2.2 (in 3d) respectively. As was explained above, in presence of the transpiration flow both models lack a small separation region in the symmetry plane of the channel, therefore a larger shift is evident: 3.1 and 2.9 (in 2d) and 2.7 and 2.6 (in 3d) respectively. Downstream of the shock wave–boundary layer interaction area ($x > 100\,\mathrm{mm}$) the disturbed profiles are subjected to a partial regeneration, reaching $H = 2.2$ (reference) and $H = 2.4$ (passive ventilation).

To the knowledge of the authors of the paper there are no other publications demonstrating numerical results (based on a solution of the Favre-averaged Navier–Stokes equations) of the passive control of the shock wave–boundary layer interaction studied experimentally in the curved duct with a local supersonic area by W. Braun (University of Karlsruhe). Therefore, in this sense the featured computational comparisons are unique. The presented SPARC solutions (utilizing the SA turbulence closure and BD transpiration model) justify a necessity of the application of dense, three-dimensional grids during the analysis of the phenomenon, assuring a satisfactory correlation with the available wind tunnel test data. The level of agreement between the experimental and CFD results is similar for the reference as for the flow control configuration, which was the main goal of the validation process. A very similar conclusion was drawn during the analysis of the passive control of the shock wave in the transonic nozzle with a flat wall described in Section 4. Achieving the secondary objective, it was proven that a topological transformation, forced by the application of the "extended" passive control method, of a single, strong, normal shock wave into a system of weaker, oblique compression and expansion waves reflecting between the convex wall and the outer edge of the supersonic region may be replicated by the numerical algorithm with confidence. This mechanism constitutes a basis of the recently proposed and investigated method of the high-speed impulsive helicopter rotor noise reduction [6].

6 NACA 0012 Airfoil with Full-Chord Perforation

The last studied test case is a flow past the quasi-2d, symmetric NACA 0012 airfoil, investigated experimentally in 8-Ft TPT (Transonic Pressure Tunnel) transonic wind tunnel at NASA Langley, with the interaction process taking place on the suction side of the profile (Figure 18). It was equipped with a full-chord ($c = 635\,\mathrm{mm}$) cavity covered by a 0.5 mm thick perforated plate of variable nominal porosity $p_{\mathrm{nom}}(x)$:

$$p_{\mathrm{nom}}(x) = p_{\mathrm{nom}}^{\mathrm{max}} \sqrt{\sin(\pi\, x/c)} \tag{7}$$

(a matrix of 368×440 normal holes of a diameter of 0.25 mm). The maximum value of $p_{\mathrm{nom}}^{\mathrm{max}} = 2.44\%$ was obtained at $x/c = 0.5$ (a surface average of $p_{\mathrm{nom}} = 1.08\%$). The test section width (distance between the side walls) was 2131 mm. The measurements were aiming at a study of the potential application of the passive control method as a mean of the automatic adaptation of the effective shape of the airfoil subjected to transpiration (displacement thickness effect) that is dependent on the current flow conditions [7]. In particular, the conditions of the aerodynamic drag reduction and the delay of the buffet onset boundary were looked after. A wide range of inflow conditions was investigated: Mach numbers Ma_∞ from 0.5 to 0.82, Reynolds numbers $Re_\infty = 2 \cdot 10^6$, $4 \cdot 10^6$, and $6 \cdot 10^6$ and nominal angles of attack α_{nom} from -1° to 6°. The laminar–turbulent transition of the boundary layer was tripped at $x/c = 0.05$. Chordwise distributions of the pressure coefficient c_{p} were measured on the surface of the model and at the bottom of the cavity. Based on the given c_{p} values the normal force c_{n} and pitching moment c_{m} coefficients were calculated.

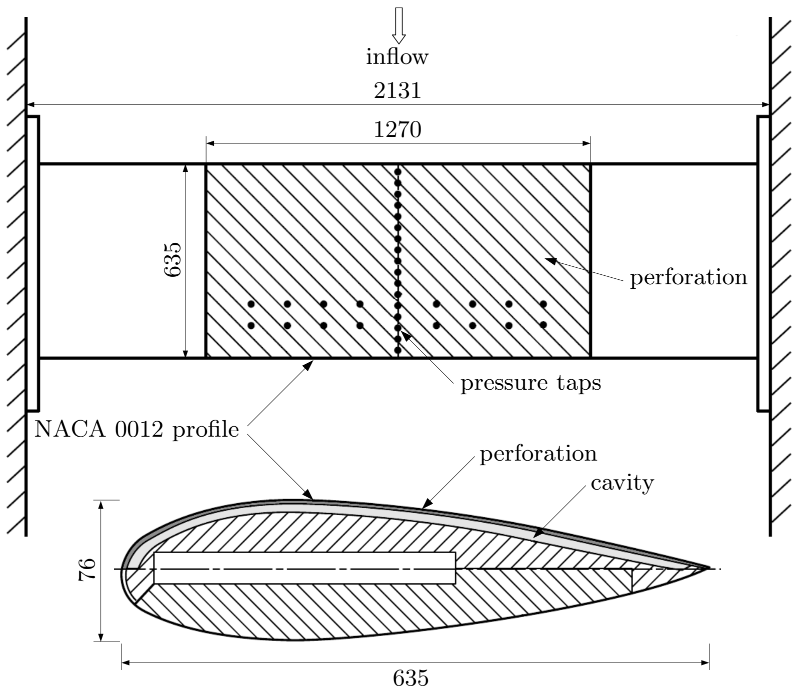

Figure 18: NACA 0012 airfoil with full-chord perforation (NASA Langley)

A wake survey system, consisting of pneumatic probes (measuring static p and stagnation p_0 pressure), was positioned $1.5\,c$ downstream the profile trailing edge. Based on the analysis of the pressure losses in the wake the drag coefficient c_d was estimated. The basic formulas describing: c_p, c_n, c_d, and c_m are as follows:

$$c_\mathrm{p} = \frac{p - p_\infty}{\frac{1}{2}\,\rho_\infty\,U_\infty^2} \quad , \quad c_\mathrm{n} = \frac{F_\mathrm{n}}{\frac{1}{2}\,\rho_\infty\,U_\infty^2\,A} \quad , \quad c_\mathrm{d} = \frac{F_\mathrm{d}}{\frac{1}{2}\,\rho_\infty\,U_\infty^2\,A} \quad , \quad c_\mathrm{m} = \frac{M_{.25}}{\frac{1}{2}\,\rho_\infty\,U_\infty^2\,A\,c} \tag{8}$$

where F_n and F_d are normal and drag components of the aerodynamic force, $M_{.25}$ is the pitching moment, A is the surface area, p_∞, ρ_∞, and U_∞ are the inflow pressure, density, and velocity respectively. Regardless of the investigated test point the stagnation value of temperature T_0 of air entering the test section was equal to 311 K. The turbulence level at the inlet was unknown. The experimental results were delivered in a row format, without application of the usual wind tunnel corrections necessary for extrapolation of the data to free-flight conditions. Finally, the polars obtained at $Ma_\infty = 0.8$ and $Re_\infty = 4 \cdot 10^6$ were chosen for a validation of the numerical implementation of the perforated wall boundary condition in SPARC.

Due to the presence of streamwise slots in the test section (designed to reduce the wind tunnel walls influence on the airfoil aerodynamic characteristics in transonic conditions) it was decided that the three-dimensional modelling was not justified from the economical point of view. Instead, a usual simplification was adopted in a form of a two-dimensional computational domain and free-flight conditions (Figure 19). Additionally, a correction of the nominal angle of attack α_nom, suggested in the 80's by C. Harris during a similar experimental investigation conducted in 8-Ft TPT with an analogous, reference NACA 0012 profile, was applied [11]. Moreover, the values of α given by the authors were lowered by $0.1°$ (i.e. $\alpha = \alpha_\mathrm{nom} + 0.1°$), which was taken into account in the simulation process. The origin of the coordinate system was positioned at the leading edge of the model. The computational domain was spanning farther than $50\,c$ from the airfoil surface in every direction. The chord length c was chosen to be equal to 1 m. In order to create a sharp (instead of the original, blunt) trailing edge a local elongation (from $x/c = 1.0$ to $x/c = 1.009$) was employed. It not only reduced the grid size, but also damped numerical instabilities associated with the appearance of the von Karman vortex street. The point of model rotation (PMR) (identical to the reference point for the pitching moment $M_{.25}$ calculation) was conventionally located at $x/c = 0.25$. A cavity covered by a perforated plate was placed on the entire suction side of the airfoil (i.e. between $x/c = 0$ and $x/c = 1.009$).

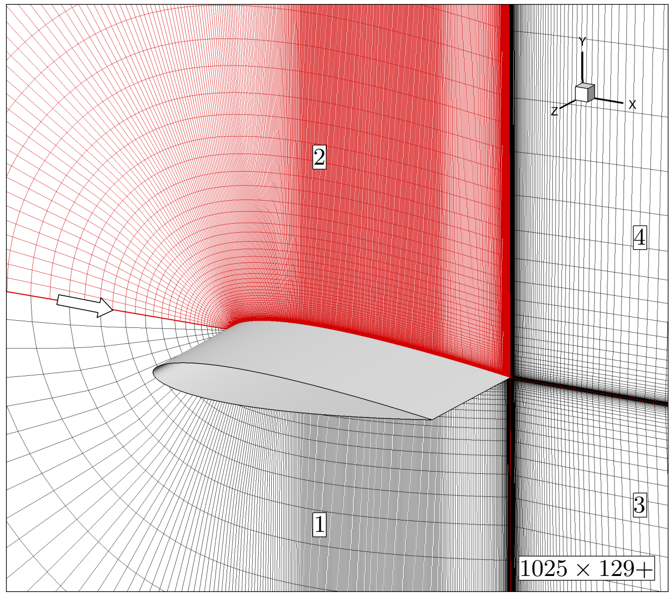

Figure 19: Numerical mesh $1025 \times 129+$ (every second line drawn, $0.4 \cdot 10^6$ of control volumes)

A base 2d mesh with standard resolution of 1025×129 ($0.2 \cdot 10^6$ volumes) was modified by a local grid refinement (4 times) of block 2, containing the shock wave–boundary layer interaction and wall ventilation regions (highlighted in red colour in Figure 19), and designated $1025 \times 129+$ ($0.4 \cdot 10^6$ volumes). For comparison purposes a globally refined (4 times) mesh 2049×257 ($0.8 \cdot 10^6$ volumes) was generated. The vertical size of the first layer of cells in the near-wall region was set to $\mathit{\Delta} y \leq 4 \cdot 10^{-6}\,\mathrm{m}$ ($y^+ \ll 1$). The adopted grid dimensions are based on the number of cells located in blocks 1 and 2 only. The values given in the brackets take into account the wake region as well (blocks 3 and 4). At the outer edge of the computational domain the subsonic far-field boundary condition was applied, with the velocity vector modulus $U_\infty = 266\,\mathrm{m\,s^{-1}}$, density $\rho_\infty = 0.260\,\mathrm{kg\,m^{-3}}$, temperature $T_\infty = 276\,\mathrm{K}$ (resulting in the inflow Mach number $Ma_\infty = 0.8$ and Reynolds number $Re_\infty = 4 \cdot 10^6$), angle of attack α from $-1°$ to $6°$, and the eddy viscosity ratio $\mu_{\mathrm{turb}}/\mu_{\mathrm{lam}} = 1$. Also the measured value of the inflow stagnation temperature $T_0 = 311\,\mathrm{K}$ was utilized. For the airfoil external solid surface (no-slip) the impermeable and adiabatic surface boundary condition was applied, interchanged with the perforated (permeable) wall boundary condition on the entire suction side (with the variable nominal porosity p_{nom} defined according to Equation (7)), in the passive control region. The temperature in the cavity T_{c} was kept constant at 311 K. Additionally, the experimental location of the boundary layer laminar–turbulent transition (tripped at $x/c = 0.05$) was fixed in the numerical model. The convergence criteria was based on a 5 orders of magnitude reduction of the density residual, accompanied by a stabilisation of the lift c_{l} and drag c_{d} coefficients of the profile and, in case of the passive control, of the pressure coefficient in the cavity $(c_{\mathrm{p}})_{\mathrm{c}}$. The grid dependency study (adopting a solution of the reference flow and exemplary $\alpha_{\mathrm{nom}} = 2°$), based on the comparison of surface pressure and friction coefficient distributions and the aerodynamic performance (c_{l}, c_{d}, and c_{m}) proved that the locally refined mesh $1025 \times 129+$ delivered accuracy of the globally refined mesh 2049×257 with half the number of control volumes.

Figure 20 presents numerical contour maps of Mach number Ma for exemplary nominal angles of attack $\alpha_{\mathrm{nom}} = 0°$, $2°$, and $4°$, revealing a transformation of the flow structure due to the application of the "global" (full-chord) passive control arrangement – the experimental visualisations are not available. The reference case corresponds to a shock wave–turbulent boundary layer interaction of medium intensity in typical high-speed conditions ($Ma_\infty = 0.8$ and $Re_\infty = 4 \cdot 10^6$). On the suction side of the airfoil a local supercritical region develops terminated by a normal compression of a decreasing strength with increasing distance from the surface – a typical behaviour often found on a transonic wing or a helicopter rotor blade. For the reference configuration and $\alpha_{\mathrm{nom}} = 0°$ (corrected to $\alpha = 0.1°$) the flow is almost symmetric in relation to the $y/c = 0$ plane, and the maximum Ma number is equal to 1.25. The height of the supersonic area

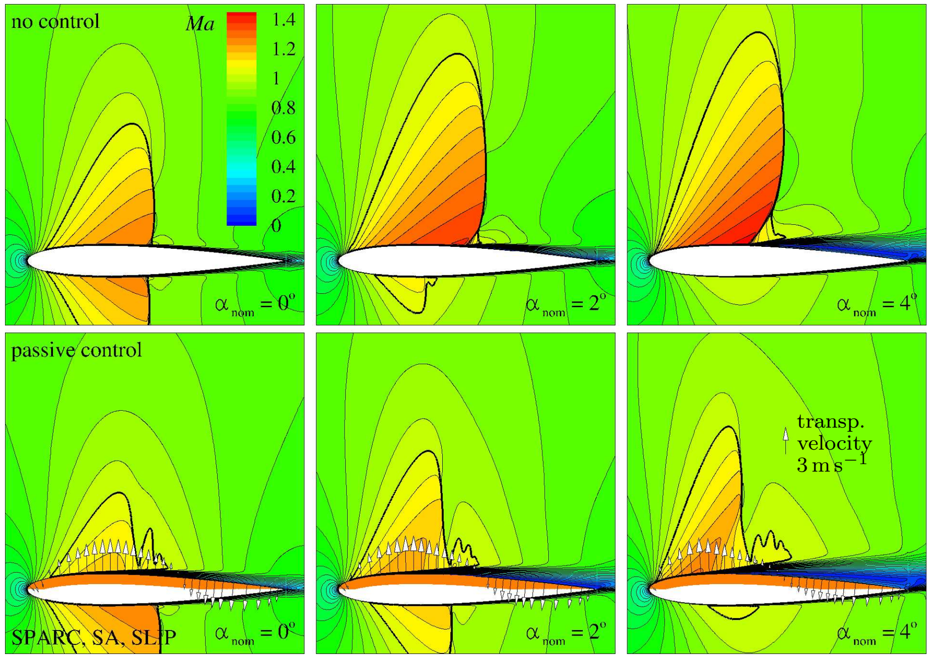

Figure 20: Numerical contour maps of Mach number Ma ($Ma_\infty = 0.8$, $Re_\infty = 4 \cdot 10^6$, and $\alpha_{\mathrm{nom}} = 0°$, $2°$, $4°$)

(marked by a thick, black line in Figure 20) is relatively low ($0.54\,c$). The shock waves, present at both sides of the profile, are weak and do not lead to separation. Increasing α_{nom} up to $2°$ (corrected to $\alpha = 1.7°$) almost causes the lower shock to cease to exist. The extent of the supercritical region grows to $0.81\,c$ (by 50%). A rise of Ma up to 1.36 results in a formation of the reversed flow area (downstream of the shock) of $30\%\,c$ length ($0.51 < x/c < 0.81$). For the last analysed $\alpha_{\mathrm{nom}} = 4°$ (corrected to $\alpha = 3.6°$) a further expansion of the $Ma > 1$ zone is visible ($0.89\,c$). The appearance of a stronger compression at $Ma = 1.42$ initiates a sudden growth of the separation bubble (to $61\%\,c$) and its extension down to the trailing edge ($x/c > 0.39$). Activation of the passive control system leads to a global modification of the flow structure. The height of the supersonic region is reduced by: 30% for $\alpha_{\mathrm{nom}} = 0°$ (corrected to $\alpha = 0.2°$), 33% for $\alpha_{\mathrm{nom}} = 2°$ (corrected to $\alpha = 1.9°$), and 29% for $\alpha_{\mathrm{nom}} = 4°$ (corrected to $\alpha = 3.8°$). In parallel, the shock intensity is significantly lowered – the maximum Ma number above the perforated wall drops to: 1.13 ($\alpha_{\mathrm{nom}} = 0°$), 1.20 ($\alpha_{\mathrm{nom}} = 2°$), and 1.26 ($\alpha_{\mathrm{nom}} = 4°$). At nominal incidences $\alpha_{\mathrm{nom}} > 0°$ a blowing from the cavity forces a generation of the reversed flow that is reaching the trailing edge. At the exemplary $\alpha_{\mathrm{nom}} = 2°$ the transpiration velocity distribution U_{t} exhibits: a short leading edge suction zone ($x/c < 0.05$, $U_{\mathrm{t}} < 1\,\mathrm{m\,s^{-1}}$), followed by more intense blowing ($0.05 < x/c < 0.56$, $U_{\mathrm{t}} < 4\,\mathrm{m\,s^{-1}}$) and again suction ($0.56 < x/c < 1.0$, $U_{\mathrm{t}} < 3\,\mathrm{m\,s^{-1}}$).

Figure 21 demonstrates the experimental and numerical characteristics of the NACA 0012 airfoil. The values of α_{nom} (uncorrected) given by R. E. Mineck and P. M. Hartwich in their report [7] have been corrected (due to the wind tunnel walls interference) in accordance with the formula earlier published by C. D. Harris [11]: $\alpha\,[°] = \alpha_{\mathrm{nom}}\,[°] - 1.55 \cdot c_{\mathrm{n}} + 0.1°$. The normal force c_{n} and pitching moment c_{m} coefficients were calculated based on the pressure coefficient c_{p} only for both, the experimental and numerical data. On the contrary, the measured and calculated drag coefficients c_{d} include contributions from pressure and friction, making the comparisons consistent. The effect of passive control is a vertical shift of the c_{n} curve towards the lower values, especially severe in the middle of the investigated incidence range (with a maximum of $\Delta c_{\mathrm{n}} = 0.192$ at $\alpha = 2.0°$). At the same time the transformation of the normal shock into a more gradual compression results in a lower c_{d} above $\alpha = 2.0°$. It is noticeable in the $c_{\mathrm{n}}\,(c_{\mathrm{d}})$ plot that at a constant c_{n} value the ventilated profile exhibits a much larger drag. The passive control action transforms the chordwise loading distribution, which is reflected by the c_{m} curve of the model, changing the character from negative (minimum of -0.014) to positive (maximum of 0.012). The results of the numerical simulations (c_{n}) of the reference and controlled profiles fit remarkably well the measurements in the entire α range. The predicted c_{d} polars satisfactorily reproduce the experimental findings for $\alpha < 2°$. Above $\alpha = 2°$ observable differences

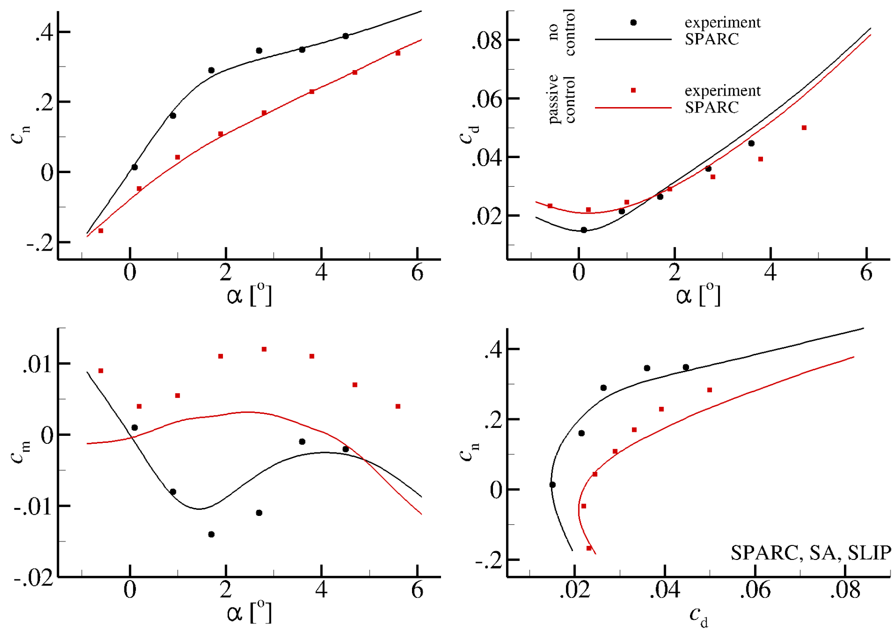

Figure 21: Normal force c_{n}, drag c_{d}, and pitching moment c_{m} coefficients ($Ma_\infty = 0.8$ and $Re_\infty = 4 \cdot 10^6$)

start to develop, reaching at most 11% ($\alpha = 3.6°$) and 22% ($\alpha = 4.7°$) for the reference and flow control cases respectively. It is worth to notice that a visible drop of c_{d} for $\alpha > 1.6°$ due to passive control is replicated by the computation. The c_{m} curve acceptably reflects the test points in the reference conditions. When the ventilation is present only the qualitative behaviour is captured with much lower values than measured. The last plot of c_{n} (c_{d}) is independent of the applied wind tunnel wall corrections.

The resulting flow recirculation through the cavity leads to a flattening of the pressure coefficient c_{p} distribution (due to the elongated compression) on the entire suction side of the airfoil (Figure 22). The depicted numerical solutions demonstrate a satisfactory level of agreement with the experimental results for both investigated configurations (with impermeable and permeable surface) and for all exemplary incidences $\alpha_{\mathrm{nom}} = 0°$, $2°$, and $4°$. Upstream of the shock wave, along the interaction region, and downstream of the compression system the prediction is equally successful. The measured mean values of the pressure coefficient in the cavity $(c_{\mathrm{p}})_{\mathrm{c}} = -0.394$, -0.435, and -0.465 (at angles of attack $\alpha_{\mathrm{nom}} = 0°$, $2°$, and $4°$) are well replicated, with the deviations reaching no more than: 0.5%, 1.6%, and 4.5% respectively.

It was proven that a transformation of a normal shock wave occurring on the NACA 0012 airfoil (NASA Langley) into a gradual compression (as a result of the "global" variant of the passive control arrangement) may be simulated numerically with confidence. The presented SPARC (SA) solutions of the base flow, obtained using 2d grids of high resolution, free-flight conditions (with proper wind tunnel corrections), and fixed laminar–turbulent transition proved to be more accurate compared to the predictions published in the available literature. Moreover, the level of agreement between the experimental and CFD results is similar for the reference as for the flow control configuration, which was the main goal of the validation.

7 Conclusions

The presented numerical results confirm that in the reference conditions (no transpiration) the SPARC (SA) code is capable of predicting the shock wave–boundary layer interaction phenomenon taking place: on a flat wall (transonic nozzle of ONERA), on a convex wall (curved duct of the University of Karlsruhe), and on an airfoil (symmetrical NACA 0012 profile of NASA Langley) with sufficient accuracy. In presence of the surface ventilation the transformation of the shock topology depends on a relative length of the passive control system ("classical", "extended", and "global" variants), leading to a large λ-foot structure, a sequence of oblique waves, or a gradual compression. The numerical algorithm (relying on the BD transpiration model)

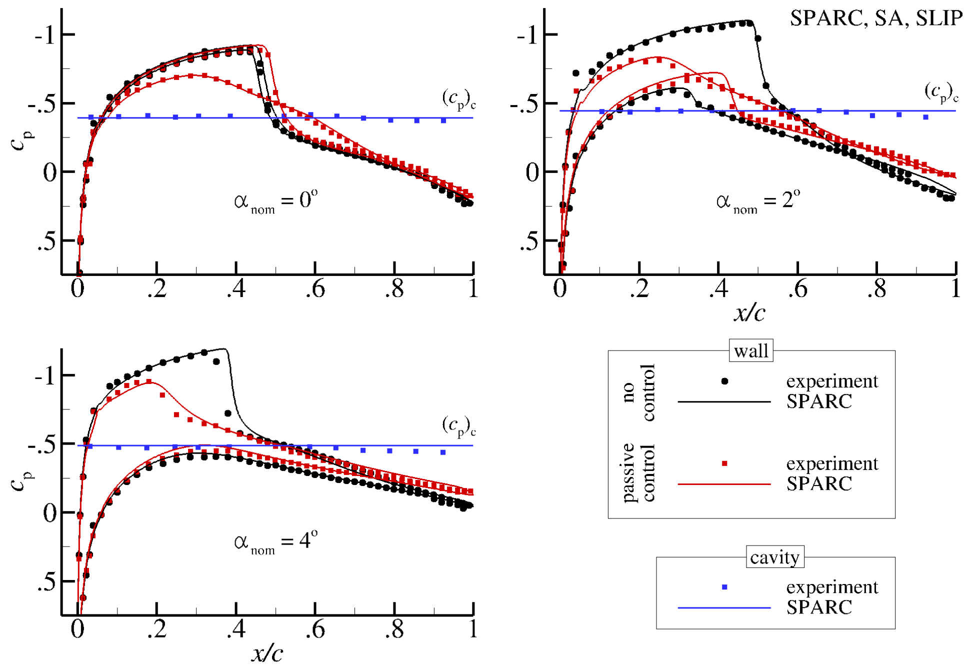

Figure 22: Surface pressure coefficient c_p distributions ($Ma_\infty = 0.8$, $Re_\infty = 4 \cdot 10^6$, and $\alpha_{nom} = 0°$, $2°$, $4°$)

is able to capture all the relevant details of such transformation, including the evolution of the boundary layer under the disturbing action of the shock and upstream blowing. A similar level of agreement between the experimental and CFD results in uncontrolled and controlled conditions validates the perforated wall boundary condition which may be used for future investigations of flow and noise control strategies.

References

[1] E. Stanewsky, J. Delery, J. Fulker and W. Geißler. *EUROSHOCK: Drag Reduction by Passive Shock Control*. Vieweg, 1997.

[2] E. Stanewsky, J. Delery, J. Fulker and P. Matteis. *Drag Reduction by Shock and Boundary Layer Control*. Springer-Verlag, 2002.

[3] P. Doerffer and R. Bohning. Modelling of perforated plate aerodynamics performance. *Aerospace Science and Technology*, 4, 2000.

[4] R. Bur, B. Corbel, J. Délery. Study of passive control in a transonic shock wave/boundary-layer interaction. *AIAA Journal*, 36(3), 1998.

[5] W. Braun. *Experimentelle Untersuchung der turbulenten Stoß-Grenzschicht Wechselwirkung mit passiver Beeinflussung*. PhD thesis, Karlsruhe University, 1990.

[6] O. Szulc, P. Doerffer and F. Tejero. Passive control of rotorcraft high-speed impulsive noise. *Journal of Physics: Conference Series*, 760, 2016.

[7] R. E. Mineck and P. M. Hartwich. Effect of full-chord porosity on aerodynamic characteristics of the NACA 0012 airfoil. Technical Paper 3591, NASA Langley, United States, 1996.

[8] F. Magagnato. KAPPA – Karlsruhe Parallel Program for Aerodynamics. *TASK Quarterly*, 2(2), 1998.

[9] R. Benay, B. Chanetz and J. Délery. Code verification/validation with respect to experimental data banks. *Aerospace Science and Technology*, 7, 2003.

[10] B. Michel. *Contribution a la simulation numerique efficace des ecoulements dans les prises d'air supersoniques*. PhD thesis, Ecole Nationale Superieure d'Arts et Metiers, Paris, France, 2004.

[11] C. D. Harris. Two-dimensional aerodynamic characteristics of the NACA 0012 airfoil in the Langley 8-Foot Transonic Pressure Tunnel. Technical Memorandum 81927, NASA Langley, United States, 1981.